


Pyruvate metabolism guides definitive lineage specification during hematopoietic emergence

Leal Oburoglu^{1,*} , Els Mansell¹, Isaac Canals² , Valgardur Sigurdsson¹, Carolina Guibentif^{1,†}, Shamit Soneji³ & Niels-Bjarne Woods^{1,**} 

Abstract

During embryonic development, hematopoiesis occurs through primitive and definitive waves, giving rise to distinct blood lineages. Hematopoietic stem cells (HSCs) emerge from hemogenic endothelial (HE) cells, through endothelial-to-hematopoietic transition (EHT). In the adult, HSC quiescence, maintenance, and differentiation are closely linked to changes in metabolism. However, metabolic processes underlying the emergence of HSCs from HE cells remain unclear. Here, we show that the emergence of blood is regulated by multiple metabolic pathways that induce or modulate the differentiation toward specific hematopoietic lineages during human EHT. In both *in vitro* and *in vivo* settings, steering pyruvate use toward glycolysis or OXPHOS differentially skews the hematopoietic output of HE cells toward either an erythroid fate with primitive phenotype, or a definitive lymphoid fate, respectively. We demonstrate that glycolysis-mediated differentiation of HE toward primitive erythroid hematopoiesis is dependent on the epigenetic regulator LSD1. In contrast, OXPHOS-mediated differentiation of HE toward definitive hematopoiesis is dependent on cholesterol metabolism. Our findings reveal that during EHT, metabolism is a major regulator of primitive versus definitive hematopoietic differentiation.

Keywords endothelial-to-hematopoietic transition; glycolysis; hematopoiesis; OXPHOS; pyruvate metabolism

Subject Categories Metabolism; Stem Cells & Regenerative Medicine

DOI 10.15252/embr.202154384 | Received 24 November 2021 | Revised 30 November 2021 | Accepted 30 November 2021 | Published online 16 December 2021

EMBO Reports (2022) 23: e54384

Introduction

In the developing embryo, primitive hematopoiesis gives rise to erythrocytes, megakaryocytes, and macrophages in the blood

islands of the yolk sac (YS) (Palis *et al*, 1999). Next, a definitive wave of hematopoiesis produces more mature erythro-myeloid (Palis *et al*, 1999) and lymphoid (Yoder *et al*, 1997; Böiers *et al*, 2013) progenitors. Around Carnegie stage (CS) 12–13, hematopoietic stem cells (HSCs) emerge in the aorta–gonad–mesonephros (AGM) region through a second definitive hematopoietic wave (Medvinsky & Dzierzak, 1996; Ivanovs *et al*, 2011). Primitive erythrocytes, erythro-myeloid progenitors (EMPs), and HSCs derive from a hemogenic endothelial (HE) cell (Lancrin *et al*, 2009; Frame *et al*, 2016; Stefanska *et al*, 2017) by a process known as endothelial-to-hematopoietic transition (EHT) (Boisset *et al*, 2010; Kissa & Herbomel, 2010). Studies on hematopoietic emergence during embryonic development have not only described EHT in spatial and temporal contexts in several animal models (Boisset *et al*, 2010; Kissa & Herbomel, 2010) but also led to a deep understanding of the growth and transcription factors regulating this process (Chen *et al*, 2009; Swiers *et al*, 2013; Zhou *et al*, 2016). Some studies of the transcriptional landscape in mouse models have hinted toward an increase in metabolic processes during HSC emergence (Zhou *et al*, 2016; Gao *et al*, 2020; Oatley *et al*, 2020). However, the role of metabolites and metabolic pathways in the emergence of hematopoietic cells has not been evaluated at length during development.

Growing evidence points to the fact that metabolic pathways can control cell fate (Folmes *et al*, 2011; Oburoglu *et al*, 2014; Mousaieff *et al*, 2015). Specifically, the fate of bone marrow (BM) HSCs is regulated by several metabolic pathways. The hypoxic niche of the BM pushes HSCs to activate a minimal energy-providing pathway, anaerobic glycolysis, and ensures their quiescent state (Takubo *et al*, 2013). HSC self-renewal and maintenance rely on fatty acid oxidation (Ito *et al*, 2012) and differentiating HSCs switch to oxidative phosphorylation (OXPHOS) to meet their energetic requirements (Simsek *et al*, 2010; Yu *et al*, 2013).

The EHT process has been modelled extensively *in vitro* using pluripotent stem cells (PSCs) and the HE intermediate which arises in this context can give rise to both primitive and definitive hematopoietic cells (Garcia-Alegria *et al*, 2018). Several studies

¹ Molecular Medicine and Gene Therapy, Lund Stem Cell Center, Lund University, Lund, Sweden

² Neurology, Lund Stem Cell Center, Lund University, Lund, Sweden

³ Molecular Hematology, Lund Stem Cell Center, Lund University, Lund, Sweden

*Corresponding authors. Tel: +46 46 222 0590; e-mail: leal.oburoglu@med.lu.se

**Corresponding authors. Tel: +46 46 222 3762; e-mail: niels-bjarne.woods@med.lu.se

[†]Present address: Sahlgrenska Center for Cancer Research, Department of Microbiology and Immunology, Institute of Biomedicine, University of Gothenburg, Gothenburg, Sweden

have focused on obtaining HE with definitive potential *in vitro* (Kennedy *et al*, 2012; Sturgeon *et al*, 2014; Ng *et al*, 2016; Sugimura *et al*, 2017), by modulating various signaling pathways, in an effort to gain further insight into definitive hematopoietic cell development to ultimately produce functional and transplantable HSCs for therapeutic use. In this study, we set out to uncover whether metabolic modulations could prompt HE cells to preferentially adopt a definitive hematopoietic fate.

As EHT implicates tight-junction dissolution, gain of stem cell-like properties and leads to extensive transcriptional and phenotypic changes in the transitioning cell (Swiers *et al*, 2013; Zhou *et al*, 2016; Guibentif *et al*, 2017), we hypothesized that metabolism contributes to regulating these processes. Previously, in animal models, the emergence of HSCs was shown to be regulated by adenosine signaling and the PKA-CREB pathway (Jing *et al*, 2015; Kim *et al*, 2015), which are tightly controlled by ATP levels and availability; suggesting a change in energy demand during EHT. Moreover, glucose metabolism was shown to induce HSC emergence in zebrafish (Harris *et al*, 2013). Here, we show a gradual and global increase in metabolism during human EHT, fueled by glucose and pyruvate. By dissecting the use of these nutrients, we uncover their roles in hematopoietic lineage specification.

Results

Recapitulation of human EHT and hematopoietic differentiation *in vitro*

In an effort to obtain both primitive and definitive hematopoietic waves in our cultures, we combined the use of two previously described small molecules during human iPSC differentiation (Fig EV1A): CHIR99021, a WNT pathway agonist which supports definitive hematopoiesis (Ng *et al*, 2016) and Activin A, which promotes primitive hematopoiesis (Kennedy *et al*, 2012). After integrating these modifications to a previously described hematopoietic differentiation protocol (Ditadi & Sturgeon, 2016), we obtained homogenic endothelial cells (HE), transitioning cells which express CD43 at intermediate levels (EHT) (Guibentif *et al*, 2017), and hematopoietic stem-like cells (HSC-like) (for gating strategies, see Fig EV1B). The HSC-like cells were termed as such as these cells are immunophenotypically similar to HSCs, but do not possess engraftment potential as demonstrated in previous studies (Kennedy *et al*, 2012; Doulatov *et al*, 2013; Elcheva *et al*, 2014; Ditadi *et al*, 2015). We characterized these three populations transcriptionally using single-cell RNA sequencing (scRNAseq). The UMAP visualization

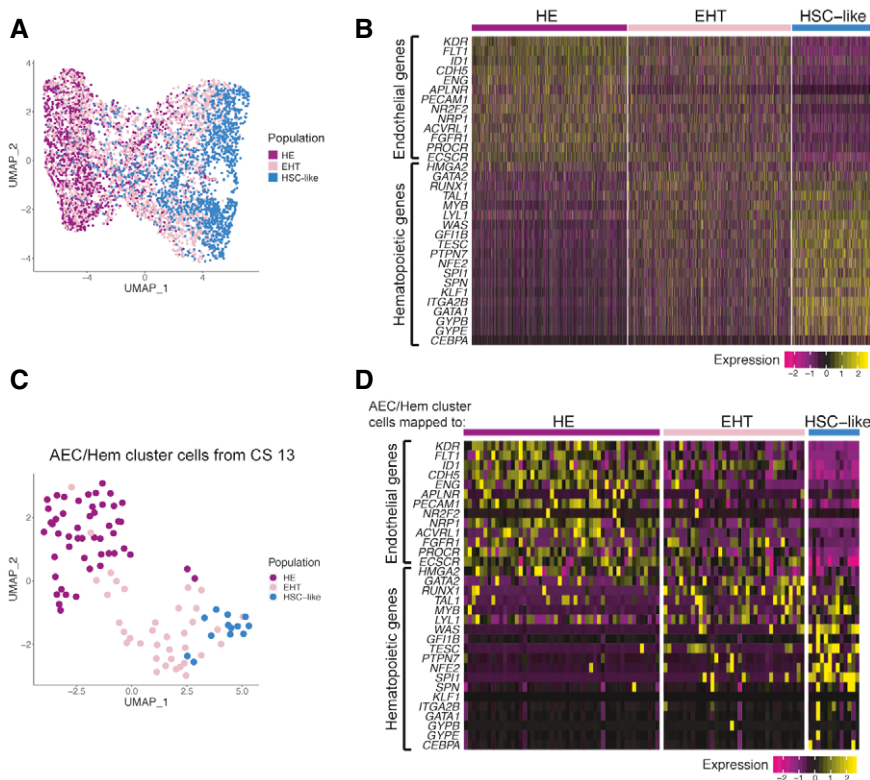


Figure 1. iPSC-derived cells match primary human EHT populations.

iPSC-derived HE, EHT, and HSC-like cells were sorted, cultured for 1 day, and analyzed by scRNAseq.

A UMAP visualization of scRNAseq data from HE, EHT, and HSC-like cells, colored by sorting phenotype.

B Heatmap showing expression levels of endothelial and hematopoietic genes in HE, EHT, and HSC-like populations.

C UMAP showing AEC/Hem cluster cells from Carnegie stage (CS) 13 (Zeng *et al*, 2019) matched against the HE, EHT, and HSC-like populations in Fig 1A.

D Heatmap showing expression levels of endothelial and hematopoietic genes in AEC/Hem cluster cells which have mapped to the HE, EHT, and HSC-like populations as shown in Fig 1C.

placed the HE cells distally from HSC-like cells, with EHT cells bridging these two populations, confirming the expected sequential EHT process (Fig 1A). Additionally, we performed a pseudotime analysis of the differentiation process in our dataset. We observed that the HSC-like cell population presented both G0 and S/G2M states and therefore, to provide a complete analysis, the pseudotime analysis was performed for both G0 and S/G2M states (Fig EV1C and D; respectively). In both cases, we observed an abundance of HE cells at the start, EHT cells in the middle, and HSC-like cells at the end of the differentiation trajectory (Fig EV1C and D; bar graphs), regardless of the cell cycle state of the cells. HE cells expressed endothelial markers, such as *KDR*, *FLT1*, *CDH5* but no hematopoietic markers; in contrast, EHT cells expressed both endothelial and hematopoietic markers and HSC-like cells only expressed hematopoietic markers, such as *RUNX1*, *TAL1*, *WAS*, and *SPN* (Fig 1B), as shown previously in other EHT systems (Swiers *et al*, 2013; Zhou *et al*, 2016; Guibentif *et al*, 2017). We generated an isolated cord blood CD34⁺ cells dataset and projected it onto our EHT process dataset using the scCoGAPS package and observed that the highest pattern weights were for pattern 1 and part of pattern 3, both encompassing our HSC-like cluster (Fig EV1E), demonstrating that cord blood CD34⁺ cells share the most transcripts with our iPSC-derived HSC-like cells. We compared our EHT process data to a recently published scRNAseq analysis of primary human embryonic cells at Carnegie stage (CS) 13 (Zeng *et al*, 2019). Of the 99 cells in the arterial endothelial and hematopoietic (AEC/Hem) clusters, 50, 36, and 13 cells mapped to our HE, EHT, and HSC-like populations, respectively (Fig 1C); and they clustered similar to our EHT dataset in Fig 1A. Furthermore, similar to our EHT dataset, AEC/Hem cluster cells mapped to HE expressed endothelial markers, such as *KDR*, *FLT1*, *CDH5*, and cells mapped to HSC-like cells expressed hematopoietic markers like *RUNX1*, *TAL1*, *WAS*, and *SPN* (Fig 1D). To rule out any bias in the data, we mapped the complete human CS 13 dorsal aorta population dataset from Zeng *et al* (2019) onto our dataset using the scCoGAPS package. We classified the resulting patterns according to the cell types described by Zeng *et al* (2019) (Table EV1) and the resulting similarity scores showed that the CS 13 endothelial cell (EC2) population mapped close to our HE cells and the CS 13 Hema cluster mapped close to both our EHT and HSC-like cells (Fig EV1F). When we assessed the relative abundance of each cell type mapping to our dataset, we observed that 58.14% of CS 13 cells clustering to our HE cells were endothelial cells (EC2) and 19.38% were hematopoietic cells (Fig EV1G). In contrast, 62.28% of CS 13 cells mapping to our EHT cells were hematopoietic cells and 25.61% were endothelial cells (EC2). Lastly, almost all cells mapping to our HSC-like cells were hematopoietic cells (92.37%). Thus, our system successfully recapitulates the human EHT process and the HE, EHT, and HSC-like populations we obtain possess hemato-endothelial transcriptional signatures equivalent to that of the cell types that occur in the human embryo at CS 13.

Next, we verified the hematopoietic potential of both HE and EHT populations. Both cell types gave rise to hematopoietic cells (CD43⁺) (Fig EV2A). At day 6 of subculture, almost all cells (> 96%) deriving from HE or EHT cells were CD43⁺ and the majority had lost CD34 expression (> 86%), pointing to their maturation. In both cell cultures, spindle-shaped endothelial cells changed their morphology to round hematopoietic cells (Fig EV2B). In both HE and EHT-derived subcultures, an erythroid (CD43⁺GPA⁺) cell

population and a non-erythroid pan-hematopoietic CD43⁺CD45⁺ cell population were clearly discernible at days 3 and 6, respectively (Fig EV2C). According to the model described by Kennedy *et al* (2012), the timeframes in which the CD43⁺GPA⁺ and the CD43⁺CD45⁺ cell populations are generated suggest their primitive and definitive natures, respectively. Moreover, the presence of embryonic (*HBZ*, *HBE1*), fetal (*HBA1*, *HBA2*, *HBG1*, *HBG2*), and adult (*HBD*, *HBB*) globin upregulation in subcultured HSC-like cells further supports that, in this setting, we obtain both primitive and definitive hematopoietic cells (Fig EV2D). Altogether, our results show that this differentiation system allows to accurately model the human EHT process and subculturing the resulting HE cells efficiently gives rise to primitive and definitive hematopoietic populations.

Glycolysis fuels distinct processes during EHT

In order to describe the metabolic processes occurring in EHT populations, we first assessed glycolysis in HE, EHT, and HSC-like cells. We observed a gradual increase in glycolytic capacity and glycolysis with differentiation (Figs 2A and EV3A). Moreover, expression of the glycolytic enzymes *HK1*, *PFKFB2*, *TP11*, *GAPDH*, *PKLR*, *ENO3*, *LDHA*, and *LDHB* as assessed by scRNAseq also increased during EHT (Fig 2B). We also observed an increase in the majority of these glycolytic enzymes during EHT in human primary cells from CS 13 (Zeng *et al*, 2019), confirming our *in vitro* results (Fig EV3B).

To understand whether glycolytic activity is required during EHT, we treated HE cells with a glucose analog, 2-Deoxy-D-glucose (2-DG), which blocks glycolysis (Fig EV3C). This treatment significantly reduced CD43⁺ cell output from HE cells at day 3 of subculture (Figs 2C and EV3D). Moreover, in the presence of 2-DG, generation of the CD43⁺GPA⁺ cell population at day 3 and the CD43⁺CD45⁺ cell population at day 6 was significantly impaired, dropping to < 50% of the control (Figs 2D and EV3E). Intriguingly, proliferation rates of EHT or HSC-like cells, but not HE, were significantly reduced in the presence of 2-DG (Figs 2E and EV3F). These results suggest that glycolysis is important for proliferation during the EHT process and as such, the use of glycolysis is required to induce hematopoietic differentiation from HE cells.

Mitochondrial respiration gradually increases during the EHT process

Along with increased glycolysis and proliferation, HSC-like cells also had increased glucose uptake compared to HE and EHT cells (Fig 2F). Interestingly, even though glycolytic flux was higher in EHT cells as compared to HE cells, glucose uptake was comparable in these two cell types. Previously, we had observed that basal respiration was higher in EHT cells compared to HE cells (Oburoglu *et al*, 2021). This result prompted us to perform a complete analysis of OXPHOS in HE versus EHT cells. We found that EHT cells displayed higher levels of not only basal respiration, but also ATP production and maximal respiration as compared to HE cells (Figs 2G and EV4A). Moreover, mitochondrial activity measured by TMRE staining was significantly increased in individually analyzed EHT cells compared to HE cells and we observed an even higher rate in the case of HSC-like cells (Fig 2H). Treatment with FCCP, which depolarizes mitochondria, abrogated the TMRE signal in all cell

types, suggesting that OXPHOS was active in these populations (Fig 2H). In line with the TMRE staining, the highest basal respiration rates we detected were in HSC-like cells (Fig 2I). Using live cell imaging by confocal microscopy, we compared mitochondrial activity in spindle-shaped HE cells versus their newly formed round

hematopoietic progeny in the same well. The TMRE staining intensity measurements showed a 2-fold higher mitochondrial activity in round as compared to spindle-shaped cells in HE wells and this value was similar to the levels detected in HSC-like cells (Fig 2J). Moreover, we observed a gradual increase in the expression of

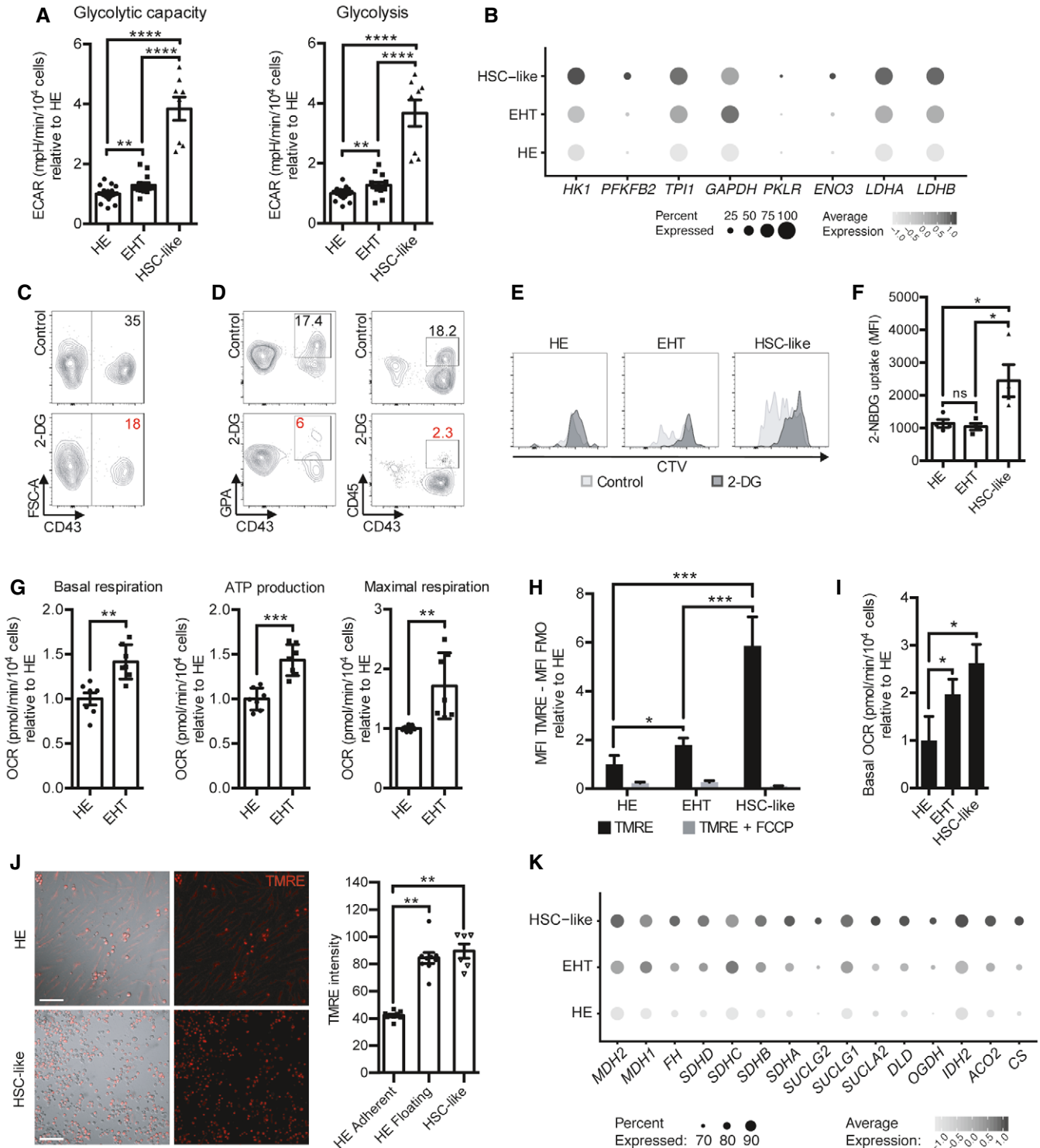


Figure 2.

Figure 2. Glycolysis, oxygen consumption, and mitochondrial activity increase during EHT.

- A Extracellular acidification rate (ECAR) was measured in HE ($n = 7$ biological replicates with 2–5 technical replicates each), EHT ($n = 7$ biological replicates with 1–3 technical replicates each), and HSC-like ($n = 3$ biological replicates with 2–4 technical replicates each) cells and glycolytic flux was assessed by extracellular flux analysis. Bar graphs show relative levels \pm SEM of the indicated processes (from 7 (HE, EHT) or 3 (HSC-like) independent experiments, unpaired t -tests).
- B Dot plots showing gene expression levels of glycolytic enzymes detected by scRNAseq and based on percent expressed (size of the dots) and average level of expression (color intensity).
- C FACS-sorted HE cells were subcultured with or without 2-DG (1 mM). Subculture day 3 representative FSC-A/CD43 plots are shown ($n = 7$ biological replicates, see Fig EV3D for bar graphs).
- D Subculture day 3 representative GPA/CD43 plots and subculture day 6 CD45/CD43 plots are shown ($n = 6$ and $n = 5$ biological replicates, respectively, see Fig EV3E for bar graphs).
- E Subculture day 3 CellTrace Violet (CTV) fluorescence was assessed by flow cytometry (representative of $n = 4$ biological replicates).
- F 2-NBDG uptake was measured by flow cytometry on day 10 for HE, EHT, and HSC-like cells and mean MFI levels \pm SEM are shown ($n = 4$ biological replicates, paired t -tests).
- G Oxygen consumption rate (OCR) was measured in HE and EHT cells ($n = 3$ biological replicates with 2–3 technical replicates each) and oxidative phosphorylation was assessed by extracellular flux analysis. Bar graphs show relative levels \pm SEM of the indicated processes (from three independent experiments; unpaired t -tests).
- H TMRE fluorescence, with or without 100 μ M FCCP treatment, was measured by flow cytometry on day 10 for HE, EHT, and HSC-like cells and MFI–MFI FMO levels \pm SEM relative to HE are shown ($n = 5$ biological replicates, paired t -tests).
- I Basal OCR was measured in day 10 HE ($n = 6$ biological replicates), EHT ($n = 5$ biological replicates), and HSC-like ($n = 4$ biological replicates) cells and bar graphs show mean levels \pm SEM relative to HE (paired t -tests).
- J Live cell imaging of HE and HSC-like cells stained with TMRE (red) at day 3 of subculture. Representative merged brightfield/TMRE and TMRE images are shown. Scale bars, 100 μ m. Bar graphs show means of TMRE staining intensity from all replicate wells across all experiments (HE spindle and HE round, $n = 3$ biological replicates with three technical replicates each; HSC-like, $n = 2$ biological replicates with three technical replicates each, Kruskal–Wallis test with multiple comparisons).
- K Dot plots showing gene expression levels of TCA cycle enzymes detected by scRNAseq and based on percent expressed (size of the dots) and average level of expression (color intensity).

Data information: ns, not significant, * $P < 0.05$, ** $P < 0.01$, *** $P < 0.001$, **** $P < 0.0001$.

several genes implicated in OXPHOS, including subunits of Complex I (genes termed *NDUF*), II (*SDHA*), IV (genes termed *COX*), and V (genes termed *ATP5*) in HE, EHT, and HSC-like populations by scRNAseq (Fig EV4B). This result was accompanied by a progressive increase in TCA cycle enzymes during EHT (Fig 2K). We observed a gradual increase in both OXPHOS-related genes and TCA cycle enzymes during EHT in human primary cells at CS 13 (Zeng *et al*, 2019), confirming our *in vitro* findings (Fig EV4C and D). Taken together, these results show that TCA cycle activity, mitochondrial respiration, and OXPHOS gradually increase during the EHT process.

Modulation of pyruvate use biases HE toward differing hematopoietic lineage outputs

As we have shown that HE cells take up glucose at similar levels as EHT cells (Fig 2F) even though their glycolytic rates are lower, we investigated whether pyruvate oxidation is important for the hematopoietic differentiation of HE cells. Pyruvate is taken up by mitochondria via the mitochondrial pyruvate carrier complex (MPC) and can be converted to acetyl-coA by the PDH enzyme to replenish the TCA cycle (Fig 3A). We blocked pyruvate entry into mitochondria using a specific MPC inhibitor called UK5099 (Fig 3A). In HE cells, unlike in EHT or HSC-like cells, MPC inhibition led to a striking increase in CD43⁺GPA⁺ cell output at day 3 of subculture (Figs 3B and EV5A). To confirm this result, we treated HE cells with an alternative molecule that also blocks pyruvate use in the TCA cycle, a PDH inhibitor (Takubo *et al*, 2013) (Fig 3A) and observed a significant increase in GPA⁺ cell output compared to the control (Fig EV5B). Furthermore, we downregulated the expression of both MPC subunits, *MPC1* and *MPC2*, using lentiviral vectors expressing shRNAs (Fig EV5C) and observed once more a 2.7-fold increase in CD43⁺GPA⁺ cell output at day 3 of subculture (Fig EV5D),

confirming our results with UK5099. We did not observe any differences in the proliferation of the GPA⁺ population deriving from HE in the presence of UK5099 as compared to the control (Fig EV5E). These results demonstrate that the use of glucose for glycolysis is sufficient to drive erythroid cell formation and that inhibiting pyruvate entry into mitochondria leads to an increased differentiation of HE cells toward the erythroid lineage. Furthermore, this biasing occurs on HE cells prior to full hematopoietic cell commitment, as demonstrated by the absence of bias when using cells downstream of the HE, such as the EHT and HSC-like populations (Fig EV5A).

Although the levels of total CD43⁺ cells were unchanged between UK5099-treated and untreated conditions at day 6 (Fig EV5F), we observed a 2-fold decrease in the CD43⁺CD45⁺ populations deriving from both HE and EHT cells, but not from HSC-like cells (Figs 3C and EV5G). Similarly, 1-AA treatment led to a significant decrease in HE-derived CD45⁺ cell population, even though total CD43⁺ cell levels were unchanged (Fig EV5H). It is important to note that UK5099 did not have an effect on the proliferation of CD45⁺ cells or on the frequency of HSC-like cells, both deriving from HE (Fig EV5I and J). These results indicate that blocking pyruvate entry into mitochondria impairs differentiation toward a CD45⁺ hematopoietic fate during EHT.

To complement these findings, we sought to induce an opposite effect by increasing pyruvate flux into mitochondria to promote TCA cycle activity and OXPHOS. Using DCA, we blocked PDKs which repress the PDH complex: this allows pyruvate to be converted to acetyl-coA and potentially fuel the TCA cycle (Fig 3A). Although the formation of CD43⁺GPA⁺ cells was not significantly altered by DCA at day 3 of HE subculture (Fig EV5K), we observed a 50% decrease in this population at day 6 in the treated condition (Figs 3D and EV5L). Thus, as DCA does not directly block glycolysis, it does not affect primitive erythroid differentiation from HE cells. Indeed, the proliferation of the GPA⁺ population deriving from

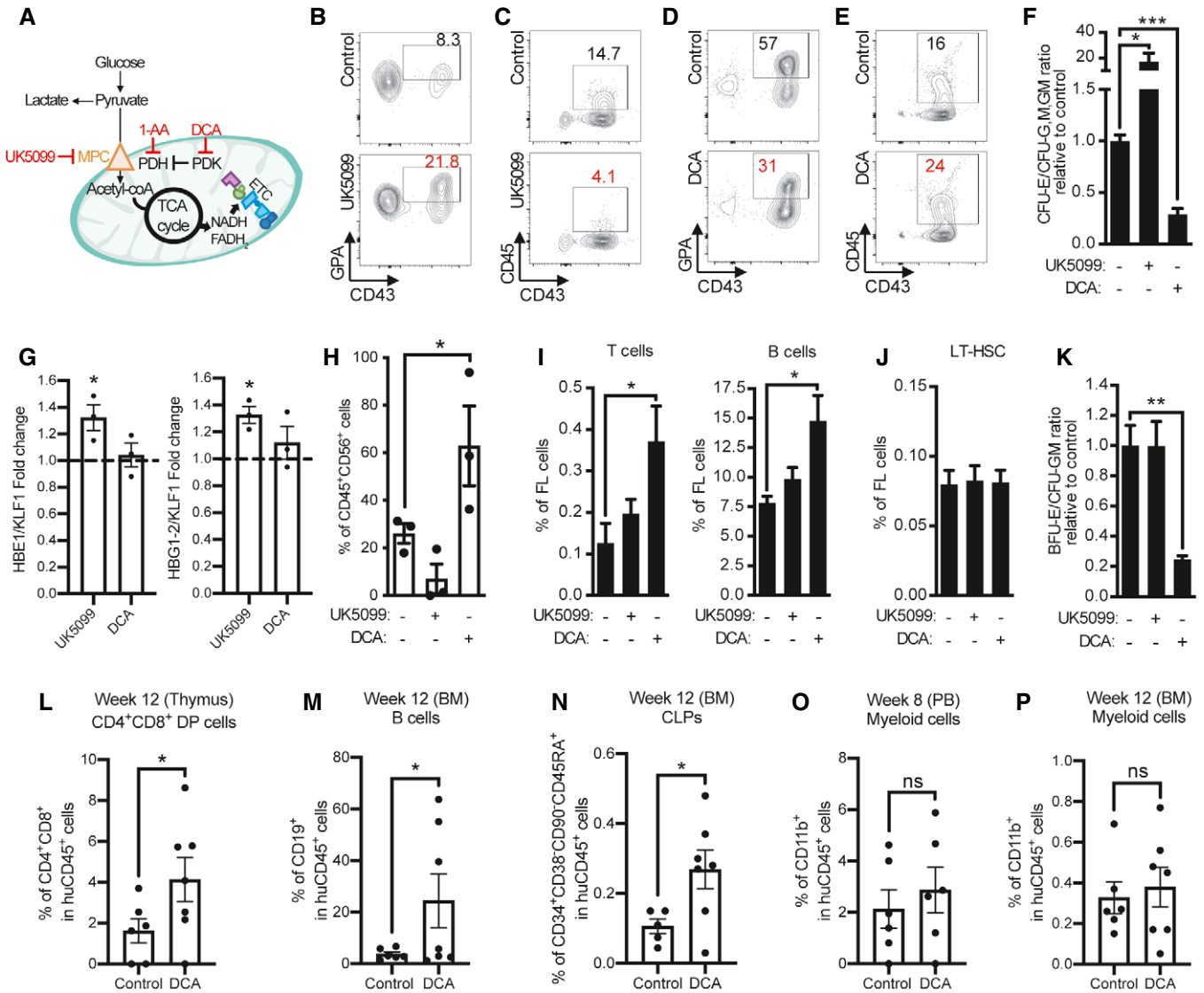


Figure 3. Increasing pyruvate flux into mitochondria in HE cells favors definitive hematopoietic differentiation.

A Pyruvate is transported into mitochondria via the mitochondrial pyruvate carrier (MPC, inhibitor: UK5099) and converted to acetyl-coA by pyruvate dehydrogenase complex (PDH, inhibitor: 1-AA). Pyruvate dehydrogenase kinases (PDKs, inhibitor: DCA) negatively regulate PDH activity.

B–E FACS-sorted HE cells were subcultured with or without UK5099 (10 μ M) or DCA (3 mM). Subculture day 3 representative GPA/CD43 plots (B, D) and subculture day 6 representative CD45/CD43 plots (C, E) are shown (see Fig EV5A and G, and L and N for corresponding bar graphs).

F Ratio of CFU-E to CFU-G, M, GM colonies \pm SEM relative to the control condition obtained from HE cells subcultured with the indicated compounds for 6 days, see Fig EV5S for percentages ($n = 5$ biological replicates with 1–2 technical replicates each, paired t -test).

G Fold change in the expression of *HBE1* or *HBG1-2* transcripts \pm SEM normalized to *KLF1* in CFUs obtained from HE cells treated with UK5099 (10 μ M) or DCA (3 mM) relative to non-treated cells ($n = 3$ biological replicates, paired t -test).

H Percentages of CD45⁺CD56⁺ \pm SEM cells obtained following 35-day co-culture of 3-day subcultured HE cells with OP9-DL1 stroma. During the 3-day subculture, HE cells were treated with the indicated compounds. ($n = 3$ biological replicates, one-way ANOVA test, see Fig EV5V for plots).

I–K Pregnant mice were injected with UK5099 or DCA at E9.5 and fetal livers were analyzed at E14.5 by flow cytometry. FL, fetal liver. Levels of T and B cells (I) and LT-HSCs (J) as percentages in fetal liver are shown for control ($n = 10$ biological replicates), UK5099-treated ($n = 14$ biological replicates), and DCA-treated ($n = 16$ biological replicates) conditions (one-way ANOVA test). (K) The ratio of BFU-E to CFU-GM colonies obtained from sorted LT-HSCs is shown (see also data in Appendix Fig S6F) (one-way ANOVA test). CFU, colony-forming unit; BFU, burst-forming unit; E, erythroid; M, macrophage; G, granulocyte.

L–P HE cells co-cultured with OP9-DL1 stroma were treated with DCA for 3 days and transplanted into irradiated NSG mice. Bone marrow (BM) and thymus were harvested on week 12. (L) The percentages \pm SEM of human CD4⁺CD8⁺ double-positive thymocytes in huCD45⁺ cells from the thymus are shown (Control, $n = 6$ biological replicates; DCA, $n = 7$ biological replicates; unpaired t -tests). The percentages \pm SEM of human B cells (M), CLPs (N) from the BM at week 12, as well as myeloid cells from PB at week 8 (O) and myeloid cells from BM at week 12 (P) in huCD45⁺ cells are shown (Control, $n = 6$ biological replicates; DCA, $n = 7$ biological replicates; unpaired t -tests). PB, peripheral blood.

Data information: ns, not significant, * $P < 0.05$, ** $P < 0.01$, *** $P < 0.001$.

the HE subculture was not affected by DCA at day 3 of subculture (Fig EV5M). Importantly, at day 6 of subculture with DCA, we observed an 80% increase in the percentage of CD43⁺CD45⁺ cells deriving from HE, but not EHT cells (Figs 3E and EV5N). Moreover, to validate this result, we downregulated the expression of PDKs using shRNAs (Fig EV5O) and while we did not note a significant effect of *PDK1*, *PDK2*, or *PDK3* downregulation, we observed a 75% increase in CD43⁺CD45⁺ cell output at day 6 of subculture following *PDK4* downregulation (Fig EV5P). This confirms our results with DCA and furthermore shows that its effect is related to blocking *PDK4* specifically. The proliferation of CD45⁺ cells or the frequency of HSC-like cells deriving from HE was not affected by DCA (Fig EV5Q and R). To assess if the changes in lineage biasing seen with the metabolic regulators was due to changes in proliferation, we also performed EdU incorporation at early time points of subculture (days 1 and 2). We found no differences in proliferation due to UK5099 or DCA treatments (Fig EV5S), further suggesting that the changes in lineage outcomes are the result of changes in the lineage potential in the HE. Taken together, these results show that when glycolysis is promoted via inhibition of pyruvate entry into the TCA cycle, HE cells preferentially give rise to erythroid cells; conversely, when pyruvate is pushed toward oxidation in mitochondria, the increased TCA cycle fueling favors CD45⁺ differentiation of HE cells.

Following 3 or 6 days of MPC inhibition with UK5099 in HE cells, we found that erythroid colony (CFU-E) formation was significantly increased compared to the untreated condition, while granulocyte and macrophage colonies were decreased (CFU-G, GM, and M) (Fig EV5T and U). In contrast, while a 3-day PDK inhibition with DCA did not have an effect on CFUs (Fig EV5U), a 6-day DCA treatment led to a decrease in CFU-Es and a significant increase in CFU-M colonies (Fig EV5T). The ratio of CFU-E colonies to the sum of CFU-G, CFU-GM, and CFU-M colonies was 20-fold higher in UK5099-treated cells and more than 3-fold lower in DCA-treated cells, as compared to the control (Fig 3F). In all conditions, we observed both bright red primitive (EryP) and brownish definitive erythroid (EryD) colonies (Fig EV5V). However, while UK5099 or DCA did not have an effect on *HBA1-2* (adult globin) expression (Fig EV5W), we observed a significant increase in *HBE1* (embryonic) and *HBG1-2* (fetal) globin transcripts in colonies obtained from UK5099-treated HE cells (Fig 3G), confirming that MPC inhibition increases generation of erythroid cells with globin gene expression associated with primitive hematopoiesis.

On the other hand, to understand whether DCA induces the formation of definitive hematopoietic cells, we induced lymphoid differentiation of day 3 HE cells in OP9-DL1 stroma co-cultures. While UK5099 treatment impaired NK cell formation, DCA treatment significantly increased NK cell differentiation as compared to untreated HE cells (Figs 3H and EV5X). Altogether, these results demonstrate that HE cells can be directed toward differing hematopoietic lineage outcomes whereby promoting pyruvate use in glycolysis (using UK5099) increases erythropoiesis with embryonic and fetal globin expression, and conversely promoting pyruvate use for OXPHOS (using DCA) increases lymphoid lineage output.

To verify these findings in an *in vivo* setting, we injected pregnant mice with UK5099 or DCA at embryonic day (E) 9.5 (Appendix Fig S1A), to influence hemogenic endothelium which gives rise to definitive hematopoiesis (both the second and third waves)

occurring at E9-9.5 and E10.5, but not primitive hematopoiesis which takes place at E7-7.25 (Medvinsky & Dzierzak, 1996; Palis *et al*, 1999). We assessed blood lineage output in embryos by characterizing the cellular composition of fetal liver (FL) at E14.5 when the FL is the prime site of hematopoiesis. We observed that hematopoietic progenitor cells (HPC)-1, which are restricted progenitors with lymphoid/myeloid potential and HPC-2, which mainly give rise to megakaryocytic progeny were significantly increased in embryos from DCA-injected mice, as compared to the control and UK5099-injected conditions (Appendix Fig S1B). In line with this, both T- and B-cell levels were increased in DCA versus control and UK5099-injected embryos (Fig 3I), supporting our *in vitro* results showing an increased CD45⁺ output with DCA. Moreover, DCA treatment led to significant decreases in stage 0, 4, and 5 erythroid populations in the FL, with no significant differences in stages 1, 2, and 3 as compared to the control and UK5099 conditions (Appendix Fig S1C and D). This profile suggests an impairment in definitive erythroid cell production (decrease in S0), while primitive erythrocytes that have formed prior to the injection are in late maturation stages in the FL (S1, 2 and 3) or have exited from the FL into the circulation (decrease in S4 and 5), as described previously (Fraser *et al*, 2007; Isern *et al*, 2008).

Furthermore, while the frequency of phenotypic long-term HSCs (LT-HSCs) defined as LSK CD48⁻CD150⁺ (Appendix Fig S1E) from the treated embryos was not significantly affected by UK5099 or DCA (Fig 3J), confirming our *in vitro* findings (Fig EV5J and R), LT-HSCs from DCA-treated embryos, did give rise to significantly more CFU-GM colonies and fewer BFU-E colonies (Appendix Fig S1F) with an 80% decrease in the BFU-E to CFU-GM ratio (Fig 3K), as compared to the control and UK5099-treated conditions. We did not see a significant effect on *in vivo* EHT and hematopoiesis by UK5099 (Fig 3I-K), confirming that MPC inhibition preferably affects the primitive hematopoietic wave. Thus, analogous to our results *in vitro*, promoting pyruvate entry to the TCA cycle by DCA increases the frequency of lymphoid/myeloid cells at the expense of mature erythroid cells *in vivo*.

In order to assess definitive hematopoietic potential of iPSC-derived cells, we intravenously injected 3-day DCA-treated HE cells co-cultured with OP9-DL1 stroma into irradiated NSG mice (Appendix Fig S1G). We obtained engraftment levels comparable to previous studies (Rahman *et al*, 2017), with around 1% human CD45⁺ cells in the peripheral blood (PB) at week 8 (Appendix Fig S1H). Intriguingly, at 12 weeks, we detected significantly more CD4⁺CD8⁺ DP thymocytes in the thymi of NSG mice injected with DCA-treated HE cells (Figs 3L and Appendix Fig S1I). Furthermore, with DCA-treated cells, we detected significantly more human B cells in the PB and BM of the NSG mice at weeks 8 and 12, respectively (Fig 3M and Appendix Fig S1J). In agreement with this, analysis of week 12 BM revealed a significant increase in the common lymphoid progenitor (CLP) population in the DCA-treated condition (Fig 3N) despite similar levels of phenotypic human HSCs (defined as CD34⁺CD38⁻CD90⁺CD49f⁺CD45RA⁻) in both conditions (Appendix Fig S1K). In contrast, the frequencies of the CD11b⁺ myeloid lineage cell were similar between the conditions (Fig 3O and P). Taken together, these transplantation results show that promoting OXPHOS by increasing pyruvate flux into mitochondria with DCA pushes HE cells toward a definitive hematopoietic phenotype with T and B potential.

Since we did not see a difference in the frequency of HSC-like cells *in vitro* (Fig EV5R), LT-HSCs *in vivo* (Fig 3J) or human HSCs deriving from transplanted HE cells *in vivo* (Appendix Fig S1K) following DCA treatment, we next sought to understand whether DCA could have an effect directly on the EHT process by affecting the numbers of resulting hematopoietic stem and progenitor cells (HSPCs). As this process takes place at E10.5 in the AGM region (Medvinsky & Dzierzak, 1996), we treated pregnant mice with DCA at E8.5 and assessed HSPC cell numbers (cKit⁺CD45⁺ cells) in the AGM regions of embryos at E10.5 (Appendix Fig S1L). We found that the numbers of cKit⁺CD45⁺ cells in control and DCA-treated embryos were similar and in the same range as previously described (Morgan *et al*, 2008) (Appendix Fig S1M). This result confirms our *in vitro* and *in vivo* results and suggests that the modulation of pyruvate metabolism has an intrinsic effect on HE cells which is inherited by HSPCs without affecting their numbers.

Pyruvate fate dictates hematopoietic lineage specification of HE cells at the single-cell level

In order to dissect the molecular effects of pyruvate manipulation on HE cells, we assessed the transcriptomic profiles of these cells at an early time point of treatment (day 2), at the single-cell level, in control and UK5099- or DCA-treated cells. First, we grouped all conditions together and separated the cells into seven clusters (Fig 4A). The majority of HE cells expressed endothelial markers, including *ENG*, *CDH5*, *PROCR*, and *ANGPT2* (Appendix Fig S2A) and their expression was mostly confined to clusters 1 through 5 (Fig 4B). In contrast, cells in clusters 6 and 7 expressed hematopoietic genes, including *RUNX1*, *GATA2*, *MYB*, and *SPN* (Fig 4B and Appendix Fig S2B). Thus, this time point most likely captures the commitment of HE cells to hematopoietic cells which occurs within clusters 6 and 7.

Focusing on isolated clusters 6 and 7 (Fig 4C), we found that an early erythropoiesis regulator, *RYK*, and erythroid-specific *KLF3* were already expressed in cluster 6 at high levels, while several other members of the erythroid transcription factor network, such as *TAL1*, *GATA2*, *ZFPM1*, *KLF1*, *NFE2*, *ANK1*, and *HBQ1*, were more highly expressed in cluster 7 (Erythroid markers; Fig 4C). Early lymphoid cell fate regulators *POU2F2* (B cell) and *GATA3* (T cell) as well as myeloid markers *SWAP70* and *IRF8* were expressed at higher levels in cluster 6, while T lymphoid *BCL11B*, myelo-monocytic *CSF1R*, *CEBPE*, and megakaryocytic *PF4* were highest in cluster 7 (Lymphoid/myeloid markers; Fig 4C). Thus, while cluster 6 cells expressed early regulators of specific lineages, cluster 7 cells started expressing transcription factors, which are part of lineage-specific transcription factor networks characteristic of more mature hematopoietic cells. Moreover, in cluster 7, the percentage of cells expressing erythroid transcription factors was > 75%, while cells expressing lymphoid or myeloid markers represented < 20% of total (Fig 4C), in accordance with the early and late emergence of GPA⁺ and CD45⁺ cells, respectively, from HE.

We found that while the percentage of cells in cluster 6 was constant between conditions, there were 38% more UK5099-treated HE cells and 35% less DCA-treated HE cells in cluster 7 compared to the control (Appendix Fig S2C). This result shows that pyruvate modulation does not affect early hematopoietic commitment (cluster 6). However, it seems to have an effect on lineage specification (cluster 7).

We then confirmed that, in clusters 6 and 7, the average expression levels of erythroid lineage genes *RYK*, *KLF3*, *TAL1*, *GATA2*, *ZFPM1*, *KLF1*, *NFE2*, *ANK1*, and *HBQ1* were higher in UK5099-treated HE cells as compared to the untreated HE cells and these factors were nearly absent in DCA-treated HE cells (left-hand dot plot, Fig 4D). In contrast, DCA-treated HE cells expressed higher levels of lymphoid/myeloid transcription factors *SWAP70*, *POU2F2*, *GATA3*, *CSF1R*, *PF4*, *BCL11B*, *CEBPE*, and *IRF8* compared to control and UK5099-treated HE cells (right-hand dot plot, Fig 4D). To further assess the effect of pyruvate manipulation on a single-cell level, we sorted single HE cells onto OP9-DL1 stroma and scored GPA⁺ clones at day 14. From a total of 552 single cells per condition, we detected 12 GPA⁺ clones in the UK5099-treated condition and 7 GPA⁺ clones in the DCA-treated condition as compared to 9 GPA⁺ clones in the control (Appendix Fig S2D). This result highly suggests the preferential differentiation of HE cells to the erythroid lineage in the presence of UK5099. Taken together, these results show that at early stages of HE differentiation, modulation of pyruvate use directly impacts the expression of lineage-specific transcription factors and affects the resulting lineage specification of HE cells.

Primitive erythroid biasing of HE during MPC inhibition relies on LSD1

Previous studies have shown that Lysine-Specific Demethylase 1 (LSD1) is essential for EHT and particularly the erythroid lineage (Takeuchi *et al*, 2015; Thambyrajah *et al*, 2016). During EHT, LSD1 acts in concert with HDAC1/2 (Thambyrajah *et al*, 2018) and GFI1/GFI1B (Thambyrajah *et al*, 2016) to induce epigenetic changes. We confirmed that HDACs are essential for EHT using an HDAC1/2 inhibitor (Trichostatin A, TSA) which impaired the emergence of CD43⁺ hematopoietic cells, as CD43 levels only reached an intermediate level, suggesting a block during EHT (Fig 5A). Moreover, we observed that *LSD1*, *GFI1*, and *GFI1B* are expressed at higher levels in UK5099-treated cells as compared to DCA-treated cells (Fig 5B), suggesting that the erythroid differentiation bias by pyruvate catabolism modulation may be LSD1 dependent. Strikingly, under conditions where LSD1 was blocked with Tranylcypromine (TCP), or downregulated by shRNAs expressed within a lentiviral vector (Appendix Fig S3A), we could not detect an increase in CD43⁺GPA⁺ cell frequency at day 3 following UK5099 treatment of HE cells (Fig 5C and D). On the other hand, TCP-treated HE cells gave rise to more CD43⁺CD45⁺ cells at day 6 similar to DCA treatment (Appendix Fig S3B); however, we determined that unlike DCA, TCP specifically increased myeloid differentiation (Appendix Fig S3C), as previously described in the literature (Schenk *et al*, 2012). Thus, mechanistically, the induction of primitive erythropoiesis through MPC inhibition is dependent on epigenetic regulation by LSD1 in HE cells.

DCA-dependent definitive hematopoiesis is promoted by cholesterol metabolism

Dichloroacetate may be directly used as a precursor of acetylation marks: acetate is converted to acetyl-coA by ACSS2 and transferred onto histones via histone acetyltransferases (HATs) (Fig 5E). Inhibiting ACSS2 did not perturb the DCA effect on CD43⁺CD45⁺ cells at day 6 of HE subculture (Fig 5F), showing that DCA is not directly

cholesterol (Fig 5I). Blocking ACC with CP-640186 (CP) had the same effect as DCA and combined treatment with both CP and DCA further increased the frequency of CD43⁺CD45⁺ cells at day 6 compared to DCA alone (Fig 5J). Thus, preventing lipid biosynthesis may increase acetyl-coA availability for cholesterol production. Indeed, in DCA-treated HE cells, we detected an increase in cholesterol content both by imaging (Fig 5K) and flow cytometry (Fig 5L)

and the latter experiment showed a dose-dependent effect of DCA on cholesterol content. Moreover, we observed higher levels of cholesterol efflux genes at day 2 in DCA-treated cells (Appendix Fig S3D), suggesting their upregulation due to the higher cholesterol content in these cells. Strikingly, treating HE cells with DCA in combination with atorvastatin (Ato) (inhibitor of the mevalonate pathway which is responsible for cholesterol biosynthesis) abrogated the

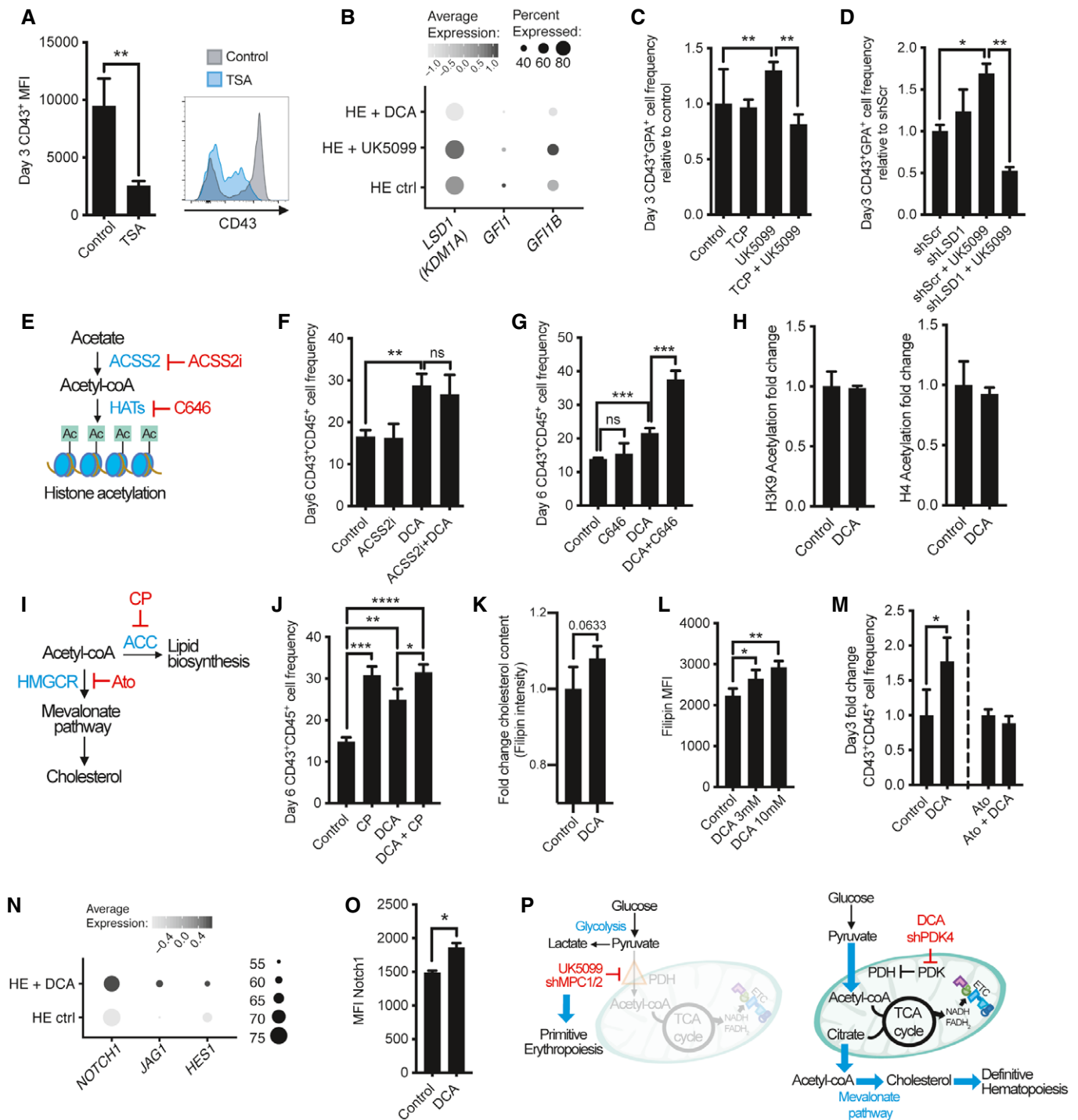


Figure 5.

Figure 5. Pyruvate catabolism affects EHT via distinct mechanisms.

- A FACS-sorted HE cells were subcultured with or without TSA (60 nM). Subculture day 3 CD43 MFI levels \pm SEM and a representative CD43 histogram are shown ($n = 3$ biological replicates 1–2 technical replicates each, paired *t*-test).
- B Dot plots showing gene expression levels of *LSD1*, *GFI1*, and *GFI1B* detected by scRNAseq and based on percent expressed (size of the dots) and average level of expression (color intensity).
- C FACS-sorted HE cells were subcultured with TCP (300 nM), UK5099 (10 μ M), or both and day 3 CD43⁺GPA⁺ cell frequencies \pm SEM relative to the control are shown ($n = 4$ biological replicates, one-way ANOVA test).
- D HE cells were transduced with shScrambled (shScr) or shLSD1 with or without UK5099 (10 μ M) the day after the sort and day 3 CD43⁺/GPA⁺ cell frequencies \pm SEM relative to shScr are presented ($n = 3$ biological replicates 1–2 technical replicates each, one-way ANOVA test).
- E Acetate can be directly converted to acetyl-coA by ACSS2 (inhibitor: ACSS2i). Acetyl-coA is the precursor of acetylation marks, transferred onto histones via histone acetyltransferases (HATs, inhibitor: C646).
- F, G FACS-sorted HE cells were subcultured with ACSS2i (5 μ M), DCA (3 mM), or both ($n = 5$ biological replicates, one-way ANOVA test) (F) or with C646 (10 μ M), DCA (3 mM), or both ($n = 3$ biological replicates, one-way ANOVA test) (G) and day 6 CD43⁺CD45⁺ cell frequencies \pm SEM are shown.
- H FACS-sorted HE cells were subcultured with or without DCA (3 mM) for 2 days on coverslips. Staining intensities of H3K9 acetylation and H4K5, 8, 12, 16 acetylation were assessed by confocal microscopy imaging and fold change \pm SEM compared to the control is shown ($n = 3$ biological replicates).
- I Acetyl-coA can be a precursor for lipid biosynthesis via ACC (inhibitor: CP-640186 or CP) or for the mevalonate pathway/cholesterol biosynthesis via HMGCR (inhibitor: Atorvastatin or Ato).
- J FACS-sorted HE cells were subcultured with CP (5 μ M), DCA (3 mM), or both and day 6 CD43⁺CD45⁺ cell frequencies \pm SEM relative to the control are shown ($n = 4$ biological replicates, one-way ANOVA test).
- K Cholesterol content \pm SEM in HE cells was measured by confocal microscopy at day 2 of DCA (3 mM) treatment by filipin III staining ($n = 3$ biological replicates, paired *t*-test).
- L Cholesterol content \pm SEM in HE cells was assessed by flow cytometry after intracellular staining with filipin III at day 3 of DCA treatment ($n = 3$ biological replicates, one-way ANOVA test).
- M FACS-sorted HE cells were subcultured with Ato (0.5 μ M), DCA (3 mM), or both and day 3 CD43⁺CD45⁺ cell frequencies \pm SEM relative to the control are shown ($n = 3$ biological replicates for control/DCA, $n = 2$ biological replicates with two technical replicates for Ato/Ato+DCA, one-way ANOVA test).
- N Dot plots showing gene expression levels of *NOTCH1*, *JAG1*, and *HES1* detected by scRNAseq and based on percent expressed (size of the dots) and average level of expression (color intensity).
- O Notch1 expression (MFI \pm SEM) in HE-derived CD43⁺CD45⁺ cells at day 3 of subculture with or without DCA (3 mM) was assessed by flow cytometry ($n = 2$ biological replicates with 1–2 technical replicates, unpaired *t*-test).
- P Glycolysis is essential for hematopoietic differentiation of HE cells and inhibiting pyruvate entry into mitochondria (via UK5099 or shMPC1/2) favors a primitive erythroid fate. Increasing pyruvate flux into mitochondria (via DCA or shPDK4) amplifies acetyl-coA production which fuels cholesterol biosynthesis and promotes definitive hematopoietic differentiation of HE cells.

Data information: ns, not significant, * $P < 0.05$, ** $P < 0.01$, *** $P < 0.001$, **** $P < 0.0001$.

effect of DCA (Fig 5M). Similarly, in zebrafish, cholesterol biosynthesis was shown to activate hematopoiesis via Notch signaling (Gu *et al*, 2019). Therefore, we assessed the expression of genes implicated in the Notch signaling pathway and observed that *NOTCH1*, *JAG1*, and *HES1* levels were higher in DCA-treated cells compared to the control (Fig 5N). Moreover, we evaluated Notch1 expression during HE subculture and strikingly, we detected an increased level of Notch1 in DCA-treated HE-derived CD43⁺CD45⁺ cells as compared to the control (Fig 5O). Taken together, our results show that DCA promotes cholesterol biosynthesis via Notch1, which favors definitive hematopoietic differentiation of HE cells (Fig 5P).

Discussion

We show here that during EHT, transitioning cells go through substantial changes in energy use and metabolism, with simultaneous increases in glycolysis and TCA cycle/OXPPOS. Previous studies in mouse models have briefly mentioned changes in metabolism when comparing endothelial cells with HSCs (Zhou *et al*, 2016; Gao *et al*, 2020; Oatley *et al*, 2020). Their findings confirm our data showing that both glycolysis and OXPPOS levels increase during EHT and suggest that this is conserved in mouse models.

We describe here a role for glucose in both glycolysis and the TCA cycle. Blocking its use with 2-DG impairs hematopoietic differentiation of HE cells. In quiescent HSCs, glycolysis was shown to be regulated by hypoxia through the stabilization of hypoxia-inducible

factor-1 α (HIF-1 α) (Takubo *et al*, 2010). Interestingly, the transition from HE to HSCs was also shown to be regulated by HIF-1 α (Harris *et al*, 2013; Imanirad *et al*, 2014). Thus, a HIF-1 α -dependent induction of glycolysis may be required for EHT.

We show here that glycolysis is sufficient to provide energy for primitive hematopoiesis. Indeed, at early embryonic stages, oxygen is not systemically available and glycolysis is the pathway of choice to produce energy (Gardner *et al*, 2000). In developing embryos, primitive erythroid cells were shown to perform high rates of glycolysis to fuel their rapid proliferation (Baron *et al*, 2012). Indeed, boosting glycolysis by blocking pyruvate entry into the mitochondria redirects HE differentiation toward primitive erythropoiesis at a very early stage of EHT, as shown by an increased frequency of erythroid transcription factor-expressing cells at the single-cell level as well as higher levels of erythroid factors and embryonic/fetal-specific globins.

In a recent study, we have shown that anaplerotic fueling of the TCA cycle by glutamine during the EHT process facilitates the differentiation of HE cells toward non-erythroid hematopoietic cells (Oburoglu *et al*, 2021). However, it remained unclear whether primitive versus definitive fate decisions were influenced or not by metabolic pathways. In this study, we have focused on pyruvate metabolism and we now unravel a role for the TCA cycle and OXPPOS in preferentially inducing definitive hematopoietic identity. We demonstrate that fueling the TCA cycle with DCA treatment leads to an increased differentiation of HE cells toward a definitive CD45⁺ lineage. While PDK inhibition with DCA does not affect

primitive erythroid cell formation, it induces definitive hematopoiesis, as measured by increased lymphoid lineage biases which we have shown both *in vitro* and *in vivo*. Remarkably, DCA treatment of HE cells leads to an increased lymphoid reconstitution, including T cells in NSG mice, confirming our hypothesis of pyruvate use being able to not only modulate erythroid and lymphoid lineage outputs but also primitive and definitive states of HE-derived cells. Our results are in agreement with previous findings in *Pdk2/Pdk4* double knockout mice, which were shown to be anemic but retained normal frequencies of T, B, and myeloid populations (Takubo *et al*, 2013). Furthermore, we show here that DCA promotes Notch1-dependent CD45⁺ cell formation by fueling cholesterol biosynthesis in HE cells. This result is corroborated by an elegant study in zebrafish demonstrating that Notch1-dependent regulation of cholesterol biosynthesis is essential for HSC emergence (Gu *et al*, 2019). Moreover, we observed that the accumulation of cholesterol in HE cells led to an increase in the expression of cholesterol efflux genes. Indeed, cholesterol efflux mechanisms have been previously shown to regulate HSPC proliferation (Yvan-Charvet *et al*, 2010), and therefore, HE cells transitioning to become HSPCs may express higher levels of cholesterol efflux genes. Thus, we now demonstrate that a direct metabolic change in HE cells, namely, increased acetyl-coA content, can promote cholesterol metabolism and control definitive hematopoietic output.

We and others have reported previously that distinct EHT cell subsets or pre-HSCs can present different lineage propensities (Zhou *et al*, 2016; Guibentif *et al*, 2017). We now demonstrate that metabolism can influence the differentiation of HE cells, suggesting that

lineage propensities may be decided at the HE level. In line with our results, a recent study combining scRNAseq with lentiviral lineage tracing revealed that cell fate biases appear at a much earlier stage during hematopoietic development than previously described with conventional methods (Weinreb *et al*, 2020). Furthermore, murine HSCs were shown to present lymphoid or myeloid hematopoietic lineage biases due to epigenetic priming which is established prior to their formation (Yu *et al*, 2016). In effect, linking epigenetic changes to metabolism is a newly emerging field which reconciliates metabolic alterations with transcriptional regulation of cellular processes. In accordance, we show here that erythroid fate induction by MPC inhibition is dependent on an epigenetic factor, LSD1. It will be of great interest to explore additional epigenetic modifications that are occurring concomitantly to the metabolic changes in EHT and how these factors contribute to specify cell fate.

To conclude, this study suggests that the lineage propensities of primitive and definitive hematopoietic waves are shaped by nutrient availability in the YS and AGM niches. Due to scarcity of oxygen in early embryonic stages, the primitive hematopoietic wave depends on glycolysis to form erythroid cells expressing embryonic globins with high affinity for oxygen (Fig 5P). This allows an efficient distribution of oxygen to newly forming tissues and promotes the use of OXPHOS, which initiates the emergence of the definitive hematopoietic waves (Fig 5P).

Ultimately, using metabolic modulators to direct definitive HSC development *in vitro* from PSCs would pave the way to produce transplantable cells, able to reconstitute the hematopoietic system of patients with hematological malignancies and disorders.

Materials and Methods

Reagents and Tools table

Reagent or resource	Source	Identifier
Taqman probes		
HBA1/2	Thermo Fisher Scientific	Hs00361191_g1
HBE1	Thermo Fisher Scientific	Hs00362216_m1
HBG2/1	Thermo Fisher Scientific	Hs00361131_g1
KLF1	Thermo Fisher Scientific	Hs00610592_m1
MPC1	Thermo Fisher Scientific	Hs00211484_m1
MPC2	Thermo Fisher Scientific	Hs00967250_m1
PDK1	Thermo Fisher Scientific	Hs01561847_m1
PDK2	Thermo Fisher Scientific	Hs00176865_m1
PDK3	Thermo Fisher Scientific	Hs00178440_m1
PDK4	Thermo Fisher Scientific	Hs01037712_m1
HPRT1	Thermo Fisher Scientific	Hs02800695_m1
Biological samples		
Human Umbilical Cord Blood samples (informed consents according to guidelines approved by the regional ethical committee)	Skåne University Hospital (Lund and Malmö) and Helsingborg Hospital	N/A
Chemicals, peptides, and recombinant proteins		
Tetramethylrhodamine, Ethyl Ester, Perchlorate (TMRE)	Thermo Fisher Scientific	Cat# T669

Reagents and Tools table (continued)

Reagent or resource	Source	Identifier
2-NBD-Glucose, Fluorescent glucose uptake probe	Abcam	Cat# ab146200
7-AAD	Sigma-Aldrich (Merck)	Cat# A9400
CHIR99021	R&D Systems	Cat# 4423/10
Activin A	R&D Systems	Cat# 338-AC
Hyclone Penicillin-Streptomycin Solution	Thermo Fisher Scientific	Cat# SV30010
UltraPure BSA	Thermo Fisher Scientific	Cat# AM2616
UK5099	Tocris (R&D Systems)	Cat# 4186
Aminoethylphosphinic acid (1-AA)	AH DIAGNOSTICS AB	Cat# SC-491938
Sodium dichloroacetate (DCA)	Sigma-Aldrich (Merck)	Cat# 347795
Trichostatin A (TSA)	Sigma-Aldrich (Merck)	Cat# T8552
<i>trans</i> -2-Phenylcyclopropylamine hydrochloride (TCP)	Sigma-Aldrich (Merck)	Cat# P8511
Ac-CoA Synthase Inhibitor (ACSS2i)	Sigma-Aldrich (Merck)	Cat# 5337560001
C646	Sigma-Aldrich (Merck)	Cat# SML0002
CP-640186	Sigma-Aldrich (Merck)	Cat# PZ0362
Atorvastatin calcium salt trihydrate	Sigma-Aldrich (Merck)	Cat# PZ0001
Oligomycin	Sigma-Aldrich (Merck)	Cat# O4876
2-Deoxy-D-glucose (2-DG)	Sigma-Aldrich (Merck)	Cat# D6134
Carbonyl cyanide 4-(trifluoromethoxy)phenylhydrazone	Sigma-Aldrich (Merck)	Cat# C2920
Rotenone	Sigma-Aldrich (Merck)	Cat# R8875
Antimycin A	Sigma-Aldrich (Merck)	Cat# A8674
Filipin III	Sigma-Aldrich (Merck)	Cat# F4767
Ammonium chloride solution	STEMCELL technologies	Cat# 07850
StemPro Accutase Cell Dissociation Reagent	Thermo Fisher Scientific	Cat# A1110501
Hyclone Penicillin-Streptomycin Solution	Thermo Fisher Scientific	Cat# SV30010
GlutaMAX Supplement	Thermo Fisher Scientific	Cat# 35050038
Recombinant Human SCF	Peprtech	Cat# 300-07
Recombinant Human IL6	Peprtech	Cat# 200-06
Recombinant Human BMP4	Peprtech	Cat# AF-120-05ET
Recombinant Human VEGF 165	Peprtech	Cat# AF-100-20
Recombinant Human GM-CSF	Peprtech	Cat# 300-03
Recombinant Human IL-3	Peprtech	Cat# 200-03
Recombinant Human FGF-basic	Peprtech	Cat# 100-18B
Recombinant Human IL-15	Peprtech	Cat# 200-15
Recombinant Human IL-7	Peprtech	Cat# 200-07
Recombinant Human IL-2	Peprtech	Cat# 200-02
Recombinant Human Flt3-L	Peprtech	Cat# 300-19
Recombinant Human IGF-I	Peprtech	Cat# 100-11
Recombinant Human IL-11	Peprtech	Cat# AF-200-11
Retacrit 10,000 IU/1 ml solution (EPO)	Hospira UK Ltd	
DMEM-F12	Thermo Fisher Scientific	Cat# 31330
StemPro-34 SFM (1X)	Thermo Fisher Scientific	Cat# 10639011
Opti-MEM Reduced Serum Medium	Thermo Fisher Scientific	Cat# 51985026
Ascorbic Acid	Sigma-Aldrich (Merck)	Cat# A4544
2-Mercaptoethanol (50 mM)	Thermo Fisher Scientific	Cat# 31350010
N2 (100x)	Thermo Fisher Scientific	Cat# 17502048

Reagents and Tools table (continued)

Reagent or resource	Source	Identifier
B27 minus ViTA (50x)	Thermo Fisher Scientific	Cat# 12587010
holo-Transferrin human	Sigma-Aldrich (Merck)	Cat# T0665
Losartan potassium	Tocris (R&D Systems)	Cat# 3798
Angiotensin II human	Sigma-Aldrich (Merck)	Cat# A9525
Recombinant Human Sonic Hedgehog/Shh	R&D Systems	Cat# 1314-SH-025/CF
FBS	Thermo Fisher Scientific	Cat# SV30160
Matrigel Matrix	Corning	Cat# 354230
TrypLE Express	Thermo Fisher Scientific	Cat# 12604-013
HyClone Phosphate Buffered Saline (PBS)	Thermo Fisher Scientific	Cat# 10462372
Critical commercial assays		
CD34 MicroBead Kit, human	Miltenyi Biotec	Cat# 130-046-703
CellTrace Violet Cell Proliferation Kit	Thermo Fisher Scientific	Cat# C34571
Chromium Single Cell 3' Reagent kit v3	10x Genomics	Cat# PN-1000075
Click-iT Edu Alexa Fluor 647 Flow Cytometry Assay Kit	Thermo Fisher Scientific	Cat# C10424
Methocult	STEMCELL Technologies	Cat# H4230
Seahorse XFe96 FluxPak mini	Agilent	Cat# 102601-100
RNeasy Mini Kit	QIAGEN	Cat# 74104
TaqMan Gene Expression Master Mix	Thermo Fisher Scientific	Cat# 4369542
NucleoBond Xtra Midi prep kit	Macherey-Nagel	Cat# 740410.50
Deposited data		
The single cell RNA sequencing data presented in this paper is available in the GEO database.		Accession number GSE141189
Experimental models: cell lines		
iPSC-CB1RB9 cell line, human (RB9-CBIPS2)	Woods <i>et al</i> (2011) STEM CELLS	PMID: 21544903
Mouse Embryonic Fibroblasts	Merck-Millipore	Cat# PMEF-NL
OP9-DL1 stroma cell line, mouse	Provided by E. Sitnicka-Quinn, Lund University, Sweden	PMID: 26287684
Experimental models: organisms/strains		
Species: Mus Musculus, strain: C57BL/6xB6.SJL, female, age: 10-14 weeks	The Jackson Laboratory	
Species: Mus Musculus, strain: C57BL/6xB6.SJL, male, age: 12-18 weeks	The Jackson Laboratory	
Species: Mus Musculus, strain: B6.SJL, male, age: 12-18 weeks	The Jackson Laboratory	
Species: Mus Musculus, strain: C57BL/6xB6.SJL × B6.SJL and C57BL/6xB6.SJL × C57BL/6xB6.SJL, female and male fetuses at E14.5 from breeding set up between the females and males specified above.	The Jackson Laboratory	
Species: Mus Musculus, strain: NOD/Cg-Prkdcscid Il2rgtm1Wjl/Szj, female, age: 8 weeks (NSG)	The Jackson Laboratory	
Software and algorithms		
FlowJo	BD Life Sciences	https://www.flowjo.com/solutions/flowjo/downloads
Wave Desktop	Agilent	https://www.agilent.com/en/products/cell-analysis/software-download-for-wave-desktop
GraphPad Prism 6	GraphPad	http://www.graphpad.com/support/faqid/%201952
FACSDiva v8.0.1	BD Bioscience	https://www.bdbiosciences.com/en-us/instruments/research-instruments/research-software/flow-cytometry-acquisition/facsddiva-software
Fiji	Image J	https://imagej.net/Fiji/Downloads

Reagents and Tools table (continued)

Reagent or resource	Source	Identifier
ZEN	Zeiss	https://www.zeiss.com/microscopy/int/products/microscope-software/zen-lite.html
Adobe Illustrator CS6	Adobe Systems Inc	https://www.adobe.com/cn/products/cs6/illustrator.html
RStudio (v1.2.1578)		https://rstudio.com/about/
Seurat package v3.1.0	Butler et al (2018) Nat Biotech; Stuart et al (2019) Cell	PMID: 29608179 PMID: 31178118
Slingshot package	Street et al (2018) BMC Genomics	PMID: 29914354
SCMAP package	Kiselev et al (2018) Nat Methods	PMID: 29608555
scCoGAPS package	Stein-O'Brien et al (2019) Cell Syst	PMID: 31121116
ca package for R (v0.71.1)		http://www.carme-n.org/

Methods and Protocols

hiPSC culture, hematopoietic differentiation, and cell isolation

The RB9-CB1 human iPSC line (Woods et al, 2011) was co-cultured with mouse embryonic fibroblasts (MEFs, Millipore), passaged every 6 days and processed to form embryoid bodies (EBs) as described previously (Guibentif et al, 2017). The differentiation protocol used in this study was previously described (Ditadi & Sturgeon, 2016); however, small modifications were made to induce both primitive and definitive hematopoiesis, as indicated below and in Fig EV1A. Newly formed EBs were first kept in SFD medium supplemented with 1 ng/ml Activin A (on days 0–2) and 3 μ M CHIR99021 (on day 2 only). At day 3, media were switched to “Day 3-SP34” medium supplemented with 1 ng/ml Activin A (on day 3 only) and 3 μ M CHIR99021 (on day 3 only) until day 6. On day 6, media were replaced by “Day 6-SP34” medium, until day 8. In some experiments where indicated, to obtain a higher yield of HSC-like cells, EBs were kept until day 10: in this case, EBs were plated onto Matrigel (8 μ g/cm², Corning)-coated dishes on day 8 and kept until day 10. Media were changed every day, except on days 5 and 7. On day 8 or 10 (as indicated), EBs were singularized with 5–6 rounds of 5-min incubations with TryPLE Express (Thermo Fisher Scientific). CD34⁺ cells were selected using the human CD34 MicroBead kit (Miltenyi Biotec) and stained with CD34-FITC, CD73-PE, VECad-PerCPCy5.5, CD38-PC7, CD184-APC, CD45-AF700, CD43-APCH7, GPA-eF450, CD90-BV605, and the viability marker 7AAD in order to sort HE (CD34⁺CD43⁻CXCR4⁻CD73⁻CD90⁺VECad⁺), EHT (CD34⁺CD43^{int}CXCR4⁻CD73⁻CD90⁺VECad⁺), and HSC-like (CD34⁺CD43⁺CD90⁺CD38⁻) cells, according to previously described markers (Choi et al, 2012; Ditadi et al, 2015; Guibentif et al, 2017).

HE, EHT, and HSC-like subculture

Sorted HE (40,000), EHT (30,000), and HSC-like (5–20,000) cells were plated onto Matrigel (16 μ g/cm², Corning)-coated 96-well flat bottom plates in HE medium (Ditadi & Sturgeon, 2016) with 1% penicillin–streptomycin and kept in a humidified incubator at 37°C, 5% CO₂, 4% O₂ overnight. The following day (day 0), wells were washed twice with PBS and fresh HE medium was added, together with 2-DG (1 mM), UK5099 (10 μ M), DCA (3 mM), TSA (60 nM),

TCP (300 nM), ACSS2i (5 μ M), C646 (10 μ M), CP-640186 (5 μ M), or Atorvastatin (0.5 μ M), where indicated. Media were changed and drugs were added every 2 days and cells were kept in a humidified incubator at 37°C, 5% CO₂, 20% O₂ for 6–7 days. Pictures were taken using an Olympus IX70 microscope equipped with a CellSens DP72 camera and CellSens Standard 1.6 software (Olympus). For single-cell subcultures, single HE cells were directly sorted with a BD FACSAriaIII onto OP9-DL1 stroma in flat-bottom 96-well plates with 120 μ l OP9 medium (OptiMEM medium with Glutamax (Invitrogen) with 10% FCS, 1% penicillin–streptomycin solution (Thermo Fisher Scientific) and 1% 2-mercaptoethanol (Invitrogen)) with SCF, IL-6, IL-11, IGF1, and EPO, and with or without 10 μ M UK or 3 mM DCA. The cells were kept in a humidified incubator at 37°C, 5% CO₂, 4% O₂ and media were replaced every 4 days. At day 14, the wells were collected and scored for GPA⁺ clones by flow cytometry, using a BD LSRII.

Extracellular flux analyses

For comparisons among HE, EHT, and HSC-like cells, day 10 FACS-sorted cells ($\geq 40,000$) were directly plated onto Seahorse XF96 Cell Culture Microplate wells coated with CellTak (0.56 μ g/well) in 2–4 replicates and extracellular flux was assessed immediately on a Seahorse XF96 analyzer. For comparisons between HE and EHT cells, day 8 FACS-sorted cells ($\geq 40,000$) were plated onto Matrigel (16 μ g/cm², Corning)-coated Seahorse XF96 Cell Culture Microplate wells in 3–4 replicates and extracellular flux was assessed 2 days after plating, on a Seahorse XF96 analyzer. To assess glycolytic flux, ECAR was measured in XF medium with 2 mM glutamine under basal conditions (after 1-h glucose starvation as per manufacturer’s instructions) as well as after the addition of 25 mM glucose, 4 μ M oligomycin, and 50 mM 2-DG and data were normalized to cell number. The levels of glycolytic capacity (ECAR_{oligomycin} – ECAR_{2-DG}) and glycolysis (ECAR_{glucose} – ECAR_{2-DG}) were calculated. To assess oxidative phosphorylation, OCR was measured in XF medium with 10 mM glucose, 2 mM glutamine, and 1 mM sodium pyruvate under basal conditions as well as after the addition of 4 μ M oligomycin, 2 μ M Carbonyl cyanide 4-(trifluoromethoxy)phenylhydrazone (FCCP), and 1 μ M rotenone/40 μ M Antimycin A and data were normalized to cell number. The levels of basal respiration

(OCR_{basal} – OCR_{Rotenone/AntimycinA}), ATP production (OCR_{basal} – OCR_{oligomycin}), and maximal respiration (OCR_{FCCP} – OCR_{Rotenone/AntimycinA}) were calculated.

Flow cytometry analyses

On days 3 and 6 of subculture, cells were collected after a 2-min incubation at 37°C with StemPro Accutase Cell Dissociation Reagent and stained with CD34-FITC, CD14-PE, CD33-PC7, CD11b-APC, CD45-AF700, CD43-APCH7, GPA-eF450, CD90-BV605, and the viability marker 7AAD and fluorescence was measured on a BD LSRII. To measure mitochondrial activity, cells were incubated with Tetramethylrhodamine ethyl ester (TMRE, 20 nM) for 30 min at 37°C. Negative controls were incubated with 100 μM FCCP for 30 min at 37°C, prior to TMRE staining. Fluorescence was measured on a BD FACSARIA III and levels of MFI–MFI FMO were calculated. To measure glucose uptake, cells were incubated with 2-(N-(7-Nitrobenz-2-oxa-1,3-diazol-4-yl)Amino)-2-Deoxyglucose (2-NBDG) for 30 min at 37°C and fluorescence was measured on a BD FACSARIA III. To measure proliferation, cells were processed with the CellTrace Violet (CTV) kit according to the manufacturer's instructions (10-min incubation) and fluorescence was measured on a BD LSRFortessa. To measure EdU incorporation, HE cells were assessed on day 1 or 2 of subculture after 24-h EdU pulses, using Click-iT EdU Flow Cytometry Cell Proliferation Assay (Thermo Fisher Scientific, C10424), according to the manufacturer's instructions. Flow cytometry outputs were analyzed on FlowJo Software, with initial gateings on SSC-A/FSC-A, FSC-H/FSC-A, SSC-H/SSC-A, and 7-AAD to exclude doublets and dead cells in all experiments.

Colony-forming unit assay

Subcultured HE cells were treated with StemPro Accutase Cell Dissociation Reagent for 2 min at 37°C and dissociated cells were resuspended in 3-ml Methocult H4230 (STEMCELL Technologies, France) (prepared according to the manufacturer's instructions, with 20-ml Iscove's Modified Dulbecco's Medium containing 2.5 μg hSCF, 5 μg GM-CSF, 2.5 μg IL-3, and 500 U EPO). Each mixture was divided into two wells of a non-tissue culture treated six-well plate. Following a 12-day incubation in a humidified incubator at 37°C, 5% CO₂, 20% O₂, colonies were morphologically distinguished and scored. For globin analysis, colonies in Methocult wells were harvested with PBS, washed thoroughly, and frozen in RLT buffer with β-mercaptoethanol. Following RNA extraction and RT (Qiagen), gene expression was assessed with taqman probes by q-PCR. The taqman probes used for this assay are HBA1/2 (Hs00361191_g1), HBE1 (Hs00362216_m1), HBG2/1 (Hs00361131_g1), and KLF1 (Hs00610592_m1).

Lymphoid differentiation assay on OP9-DL1 stroma

Subculture day 3 HE cells cultured in the presence of UK5099 (10 μM) or DCA (3 mM), as indicated, were collected after a 2-min incubation at 37°C with StemPro Accutase Cell Dissociation Reagent and seeded onto 80% confluent OP9-DL1 stroma. Cells were cultured in OP9 medium (OptiMEM medium with Glutamax (Invitrogen) with 10% FCS, 1% penicillin–streptomycin solution (Thermo Fisher Scientific) and 1% 2-mercaptoethanol (Invitrogen)) with SCF (10 ng/ml), FLT3-L (10 ng/ml), IL-2 (5 ng/ml), IL-7 (5 ng/ml, first 15 days only), and IL-15 (10 ng/ml) with passaging onto new OP9-DL1 stroma every week, as described previously

(Renoux *et al.*, 2015). At day 35 of co-culture, cells were analyzed on a BD LSRFortessa.

Single-cell RNAseq library preparation and sequencing

Sorted HE, EHT, and HSC-like cells as well as magnetically selected (Miltenyi Biotec) cord blood CD34⁺ cells were plated onto Matrigel (16 μg/cm², Corning)-coated 96-well flat bottom plates in HE medium (Ditadi & Sturgeon, 2016) with 1% penicillin–streptomycin and kept in a humidified incubator at 37°C, 5% CO₂, 4% O₂ overnight. The following day (day 0), wells were washed twice with PBS and fresh HE medium was added, together with UK5099 (10 μM) or DCA (3 mM), where indicated. On day 1 and day 2 (as indicated), cells were washed twice with PBS 0.04% UltraPure BSA and collected after a 2-min incubation at 37°C with StemPro Accutase Cell Dissociation Reagent. Cells were spun down, resuspended in PBS 0.04% UltraPure BSA, counted (yield between 8,000 and 18,000 cells), and library preparation was conducted according to the Chromium Single Cell 3' Reagent kit v3 instructions (10x Genomics). Sequencing was performed on a NOVASeq 6000 from Illumina with the run parameters (28-8-0-91) recommended by 10x Genomics with a final loading concentration of 300 pM of the pooled libraries. Human Umbilical Cord Blood samples were collected from Skåne University Hospital (Lund and Malmö) and Helsingborg Hospital with informed consents according to the guidelines approved by the regional ethical committee.

Single-cell RNAseq analysis

The data were processed and analyzed using Seurat v3.1.0, where cells were allowed to have up to 20% mitochondrial reads prior to log normalization and finding the top 500 variable genes using the “vst” method. Cell cycle scores were calculated and the data were scaled regressing on mitochondrial content and the difference of the S and G2M score. Principal components were calculated prior to calculating a UMAP. Cell IDs, the UMAP, phase, and cell type are provided in Dataset EV1. Pseudotime trajectories describing two developmental routes were identified in our EHT dataset using Slingshot (Street *et al.*, 2018) along which the cells were ordered. The cells were then binned along each trajectory where the cell-type composition of each bin was calculated as percentages. Cord blood CD34⁺ cells were mapped to our data and labeled using scCoGAPS (Stein-O'Brien *et al.*, 2019). CS13 data from Zeng *et al.* (2019) were read and processed to make a UMAP from which the cells they name as “AEC” and “Hem” were identified. These 99 cells were mapped to our data and labeled using SCMAP (Kiselev *et al.*, 2018). Carnegie Stage 13 data from Zeng *et al.* (2019) were mapped to our EHT dataset using scCoGAPS where 10 patterns were identified, named according to their respective weights (as shown in Table EV1) and then projected using projectR. Each cell was assigned to the group that achieved the highest weight. An overview showing the relationship between cell types and patterns was done by forming a contingency table on which correspondence analysis was performed using the ca package for R. Differentially expressed genes were found using the FindAllMarkers function. Cell numbers for day 1 samples are as follows: HE = 1,451, EHT = 1,523, HSC-like = 732. Cell numbers for day 2 samples are as follows: HE ctrl = 1,195, HE + UK5099 = 718, HE + DCA = 2,309. All assessed endothelial and hematopoietic genes were previously used in several publications to validate the EHT process (Swiers *et al.*, 2013; Ng

et al, 2016; Zhou et al, 2016; Guibentif et al, 2017). For gene expression analyses, gene sets for glycolysis, oxidative phosphorylation, and cholesterol efflux were downloaded from The Molecular Signatures Database (MSigDB).

Downregulation via shRNAs

Short-hairpin sequences recognizing the genes of interest were cloned into GFP-expressing pRRL-SFFV vectors, embedded in a microRNA context for minimal toxicity, as described previously (Fellmann et al, 2013). Each lentivirus batch was produced in two T175 flasks of HEK 293T cells by co-transfecting 22 µg of pMD2.G, 15 µg of pRSV-Rev, 30 µg of pMDLg/pRRE, and 75 µg of the shRNA vector using 2.5 M CaCl₂. Medium was changed 16 h after transfection and viruses were harvested 48 h after transfection, pelleted at 20,000 g for 2 h at 4°C, resuspended in 100 µl DMEM, aliquoted, and kept at -80°C. The downregulation efficiency of each shRNA was measured by assessing the corresponding gene expression by qPCR in sorted GFP⁺ cells, 3 days after lentiviral transduction of cord blood CD34⁺ HSPCs. The taqman probes used for this assay are MPC1 (Hs00211484_m1), MPC2 (Hs00967250_m1), PDK1 (Hs01561847_m1), PDK2 (Hs00176865_m1), PDK3 (Hs00178440_m1), PDK4 (Hs01037712_m1), LSD1/KDM1A (Hs01002741_m1), and HPRT1 (Hs02800695_m1). HE cells were transduced by direct addition of lentivirus particles into the culture medium on the day after the sort.

In vivo compound injections and murine hematopoiesis assessment

For fetal liver analysis, pregnant female C57Bl/6xB6.SJL mice were injected intraperitoneally at E9.5 with UK5099 (4 mg/kg) or DCA (200 mg/kg) or PBS (control). Embryos were harvested at E14.5 and individually weighed and processed. Fetal livers were dissected and homogenized in 800-µL ice-cold PBS supplemented with 2% fetal bovine serum (FBS) and FL cells were washed in PBS with 2% FBS. For the differentiated lineage panel, cells were stained with B220 and CD19 (B-cell markers)- PE, CD3e-APC, Ter119-PeCy7, and CD71-FITC and analyzed on a BD FACSAria III. For the HSC panel, samples were first treated with ammonium chloride solution (STEMCELL Technologies, France) to lyse red blood cells, washed twice in ice-cold PBS with 2% FBS, stained with CD3e, B220, Ter119, Gr1 (Lineage)- PeCy5, c-Kit-Efluor780, Sca1-BV421, CD48-FITC, CD150-BV605, and 7-AAD (for dead cell exclusion), and analyzed on a BD FACSAria III. Flow cytometry outputs were analyzed on FlowJo Software, with initial gatings on SSC-A/FSC-A and FSC-H/FSC-A to exclude doublets. For plating of CFU assays, 100 LT-HSCs were sorted (gating strategy shown in Appendix Fig S1E) and resuspended in 3.0 ml Methocult M3434 (STEMCELL Technologies, France). Each mixture was divided onto two wells of a non-tissue culture treated six-well plate. Following a 14-day incubation in a humidified incubator at 37°C, 5% CO₂, 20% O₂, colonies were morphologically distinguished and scored. For AGM analysis, pregnant female C57Bl/6xB6.SJL mice were injected intraperitoneally at E8.5 with DCA (200 mg/kg) or PBS (control). Embryos were harvested at E10.5 and their AGM regions were individually processed as described previously (Fang et al, 2016). Briefly, AGM regions were dissected and digested with Collagenase II (Life Technologies) in PBS supplemented with 10% fetal bovine serum (FBS) and cells in single-cell suspension were washed in PBS with 10% FBS. Cells

were stained with anti-cKit and anti-CD45 antibodies and analyzed on a BD LSRFortessa. Experiments and animal care were performed in accordance with the Lund University Animal Ethical Committee.

NSG mice transplantations

Sorted human HE cells (350,000) were mixed with OP9-DL1 stroma (60,000) and subcultured for 3 days with or without DCA (3 mM) on Matrigel (16 µg/cm², Corning)-coated 12-well plates in HE medium (Ditadi & Sturgeon, 2016). Between 100,000 and 150,000 cells from control or DCA samples were transplanted into sublethally irradiated (300 cGy) 8-week-old female NOD/Cg-Prkdc^{scid} Il2rg^{tm1Wjl}/SzJ mice (NSG, The Jackson Laboratory) together with 20,000 whole BM support cells from C57Bl/6.SJL mice (CD45.1⁺/CD45.2⁺, in house breeding). Cells were transplanted in single-cell solution in 250-µl PBS with 2% FBS through intravenous tail vein injection. Drinking water of transplanted NSG mice was supplemented with ciprofloxacin (125 mg/l, HEXAL) for 3 weeks after transplantation to prevent infection. Mice were housed in a controlled environment with 12-h light-dark cycles with chow and water provided ad libitum. Experiments and animal care were performed in accordance with the Lund University Animal Ethical Committee.

Peripheral blood analysis after NSG mice transplantations

Peripheral blood (PB) was collected from the tail vein into EDTA-coated microvette tubes (Sarstedt, Cat# 20.1341.100). Peripheral blood was lysed for mature erythrocytes in ammonium chloride solution (STEMCELL technologies) for 10 min at room temperature, washed and stained for cell surface antibodies for 45 min at 4°C, washed, and filtered prior to flow cytometry analysis on the FACS AriaIII (BD). Flow cytometry outputs were analyzed on FlowJo Software, with initial gatings on SSC-A/FSC-A and FSC-H/FSC-A for doublet exclusion, on DAPI for dead cell exclusion and on huCD45/muCD45.1 for murine cell exclusion.

Bone marrow analysis after NSG mice transplantations

Bone marrow was analyzed at the 12-week transplantation endpoint. Mice were euthanized by spinal dislocation followed by the dissection of both right and left femurs, tibias, and iliac bones. Bone marrow was harvested through crushing with a pestle and mortar and cells were collected in 20-ml ice-cold PBS with 2% FBS, filtered, and washed (350 g, 5 min). Bone marrow cells were lysed for red blood cells (ammonium chloride solution, STEMCELL technologies) for 10 min at room temperature, washed and stained for cell surface antibodies for 45 min at 4°C, washed, and filtered prior to FACS analysis on the FACS AriaIII (BD). Flow cytometry outputs were analyzed on FlowJo Software, with initial gatings on SSC-A/FSC-A and FSC-H/FSC-A for doublet exclusion, on DAPI or 7AAD for dead cell exclusion and on huCD45/muCD45.1 for murine cell exclusion.

Thymus analysis after NSG mice transplantations

Whole thymus was harvested at the 12-week transplantation endpoint. The thymocytes were mechanically dissociated from connective tissue in the thymus by pipetting up and down in PBS with 2% FBS, followed by filtration through a 50-µm sterile filter. Erythrocyte contamination was removed by lysing the sample in ammonium chloride solution (STEMCELL technologies) for 10 min at room temperature. Samples were washed and spun down after and the pellet

of thymocytes was resuspended in FACS buffer and stained for cell surface antibodies for 45 min at 4°C, washed, and filtered prior to FACS analysis on the FACS AriaIII (BD). Flow cytometry outputs were analyzed on FlowJo Software, with initial gatings on SSC-A/FSC-A and FSC-H/FSC-A for doublet exclusion, on DAPI for dead cell exclusion and on huCD45/muCD45.1 for murine cell exclusion.

Confocal microscopy imaging and quantification

For TMRE staining, on day 3 of subculture, half of the culture medium was removed and cells were stained with 20 nM TMRE (Thermo Fisher Scientific, T669) by direct addition into the culture medium of a 2x concentrated solution. After a 20-min incubation at 37°C, wells were carefully washed with PBS and fresh HE medium was added. During acquisition, cells were kept in a humidified incubator at 37°C, 5% CO₂, 20% O₂. For immunocytochemistry, subculture day 2 HE cells (plated on coverslips) were washed twice in PBS, fixed with 4% PFA for 15 min at RT, and washed three times with PBS. For filipin staining, fixed cells were incubated with 100 µg/ml filipin III (Sigma-Aldrich, F4767) for 1 h, washed three times with PBS, and rinsed with distilled water before mounting with PVA/DABCO. For H3K9 and H4 acetylation staining, fixed cells were permeabilized and blocked 1 h at RT with PBS + 0.25% Triton X-100 + 5% normal donkey serum (blocking solution) followed by incubation overnight at 4°C with primary antibodies diluted in blocking solution. Cells were then washed 2 × 5 min with PBS + 0.25% Triton X-100 (TPBS) and 5 min with blocking solution before incubation with secondary antibodies 2 h at RT diluted in blocking solution. Cells were later washed 5 min with TPBS containing 1 µg/ml Hoechst and twice with PBS before being rinsed with distilled water and mounted with PVA:DABCO. Images were obtained with the 10x (TMRE) or 20x (Filipin and acetylation) objective of a Zeiss LSM 780 confocal microscope using the Zen software and a 1.5× zoom (TMRE) or 0.6× zoom (Filipin and acetylation). Acquisition settings were the same for all images of each experiment, taking the same number of stacks. Intensity quantification was performed using the Fiji software as follows. For TMRE, using the brightfield channel, ROIs were selected for five spindle-shaped and five round cells (randomly chosen) and average intensity for each ROI was calculated in a summatory Z-stack of the TMRE channel. For filipin and acetylation, the summatory Z-stack for the filipin channel was obtained and average intensity calculated. A total of 2–3 independent experiments with 2–3 replicate wells were quantified. For each replicate well, 4–6 images were acquired.

Statistical analyses

Significance of differences between conditions were calculated using paired/unpaired *t*-tests, one/two-way analysis of variance (ANOVA) tests, or Kruskal–Wallis tests with multiple comparisons in GraphPad Prism 6 software, as indicated. *P* values are indicated in figures with the following abbreviations: ns, not significant, **P* < 0.05, ***P* < 0.01, ****P* < 0.001, *****P* < 0.0001.

Data availability

The single-cell RNA sequencing data presented in this paper are publicly available in the GEO database under the accession number

GSE141189 and using the following link: <https://www.ncbi.nlm.nih.gov/geo/query/acc.cgi?acc=GSE141189>.

Expanded View for this article is available online.

Acknowledgements

We are grateful to Qianren Jin and Emanuela Monni for their help in the human ES/iPS Core facility. We thank Ulrich Pfisterer, Eva Erlandsson, Linda Geirsonson Ulfsson, and Björn Hallström at the Single-Cell Genomics Platform for performing sample/library preparation and sequencing at the Center for Translational Genomics. We are grateful to Ludwig Schmderer for providing cord blood CD34⁺ cells. We thank the StemTherapy FACS Core Facility at the Lund Stem Cell Center for their precious help. We thank Eskil Elmer for sharing the use of the Seahorse XF96 Analyzer. We thank Gladys Telliam and Ewa Sitnicka-Quinn for providing the OP9-DL1 cell line. We are indebted to Kristijonas Žemaitis, David Yudovich, Kenichi Miharada, Xiaojie Xian, and Filipe Pereira for valuable advices and helpful discussions. LO has been supported by Wenner-Gren Stiftelserna (utländsk postdoktor), EMBO Long-Term Fellowship (ALTF 1437-2016), and BioCARE – A Strategic Research Area at Lund University. EM has been supported by Knut och Alice Wallenbergs Stiftelse (500531-1591), Barncancerfonden (PR2019-0099), and Vetenskapsrådet (2019-01752). IC is supported by Svenska Sällskapet för Medicinsk Forskning (SSMF) Stora Anslag (S20-0003). This work was generously funded by grants from the Cancerfonden (CAN 2015/801, CAN 2017/672 and 20 1250 PjF), Vetenskapsrådet (2016-03020), BioCARE, and the Royal Physiographic Society of Lund (Fysiografen, Endowments for the Natural Sciences, Medicine and Technology – Medicine, 39542). Open access funding enabled and organized by ProjektDEAL.

Author contributions

LO and N-BW conceived and designed the study. LO performed experiments, analyzed, and interpreted the data. LO and N-BW conceptualized the results of the study. EM designed and carried out *in vivo* murine experiments. IC acquired and analyzed confocal microscopy data, produced lentiviral particles and performed AGM region extractions. VS set up mouse breeding and performed *in vivo* compound injections. CG contributed to setting up the hematopoietic differentiation protocol. SS processed and analyzed single-cell RNAseq data. LO wrote the original draft, all authors reviewed and edited the manuscript. LO and N-BW acquired the funding.

Conflict of interest

N-BW is a co-founder and shareholder of Amniotics AB, Lund, Sweden. The remaining authors declare no conflict of interests.

References

- Baron MH, Isern J, Fraser ST (2012) The embryonic origins of erythropoiesis in mammals. *Blood* 119: 4828–4837
- Böiers C, Carrelha J, Lutteropp M, Luc S, Green J, Azzoni E, Woll P, Mead A, Hultquist A, Swiers G *et al* (2013) Lymphomyeloid contribution of an immune-restricted progenitor emerging prior to definitive hematopoietic stem cells. *Cell Stem Cell* 13: 535–548
- Boisset J-C, van Cappellen W, Andrieu-Soler C, Galjart N, Dzierzak E, Robin C (2010) *In vivo* imaging of haematopoietic cells emerging from the mouse aortic endothelium. *Nature* 464: 116–120
- Butler A, Hoffman P, Smibert P, Papalexi E, Satija R (2018) Integrating single-cell transcriptomic data across different conditions, technologies, and species. *Nat Biotechnol* 36: 411–420

- Chen MJ, Yokomizo T, Zeigler BM, Dzierzak E, Speck NA (2009) Runx1 is required for the endothelial to haematopoietic cell transition but not thereafter. *Nature* 457: 887–891
- Choi K-D, Vodyanik M, Togarrati P, Suknuntha K, Kumar A, Samarjeet F, Probasco M, Tian S, Stewart R, Thomson J et al (2012) Identification of the hemogenic endothelial progenitor and its direct precursor in human pluripotent stem cell differentiation cultures. *Cell Rep* 2: 553–567
- Ditadi A, Sturgeon CM, Tober J, Awong G, Kennedy M, Yzaguirre AD, Azzola L, Ng ES, Stanley EG, French DL et al (2015) Human definitive haemogenic endothelium and arterial vascular endothelium represent distinct lineages. *Nat Cell Biol* 17: 580–591
- Ditadi A, Sturgeon CM (2016) Directed differentiation of definitive hemogenic endothelium and hematopoietic progenitors from human pluripotent stem cells. *Methods* 101: 65–72
- Doulatov S, Vo LT, Chou SS, Kim PG, Arora N, Li H, Hadland BK, Bernstein ID, Collins JJ, Zon LI et al (2013) Induction of multipotential hematopoietic progenitors from human pluripotent stem cells via re-specification of lineage-restricted precursors. *Cell Stem Cell* 13: 459–470
- Elcheva I, Brok-Volchanskaya V, Kumar A, Liu P, Lee J-H, Tong L, Vodyanik M, Swanson S, Stewart R, Kyba M et al (2014) Direct induction of haematoendothelial programs in human pluripotent stem cells by transcriptional regulators. *Nat Commun* 5: 1–11
- Fang JS, Gritz EC, Marcelo KL, Hirschi KK (2016) Isolation of murine embryonic hemogenic endothelial cells. *J Vis Exp* 112: e54150
- Fellmann C, Hoffmann T, Sridhar V, Hopfgartner B, Muhar M, Roth M, Lai D, Barbosa IAM, Kwon J, Guan Y et al (2013) An optimized microRNA backbone for effective single-copy RNAi. *Cell Rep* 5: 1704–1713
- Folmes CDL, Nelson TJ, Martinez-Fernandez A, Arrell DK, Lindor JZ, Dzeja PP, Ikeda Y, Perez-Terzic C, Terzic A (2011) Somatic oxidative bioenergetics transitions into pluripotency-dependent glycolysis to facilitate nuclear reprogramming. *Cell Metab* 14: 264–271
- Frame JM, Fegan KH, Conway SJ, McGrath KE, Palis J (2016) Definitive hematopoiesis in the yolk sac emerges from Wnt-responsive hemogenic endothelium independently of circulation and arterial identity. *Stem Cells* 34: 431–444
- Fraser ST, Isern J, Baron MH (2007) Maturation and enucleation of primitive erythroblasts during mouse embryogenesis is accompanied by changes in cell-surface antigen expression. *Blood* 109: 343–352
- Gao P, Chen C, Howell ED, Li Y, Tober J, Uzun Y, He B, Gao L, Zhu Q, Siekmann AF et al (2020) Transcriptional regulatory network controlling the ontogeny of hematopoietic stem cells. *Genes Dev* 34: 950–964
- Garcia-Alegria E, Menegatti S, Fadlullah MZH, Menendez P, Lacaud G, Kouskoff V (2018) Early human hemogenic endothelium generates primitive and definitive hematopoiesis *in vitro*. *Stem Cell Reports* 11: 1061–1074
- Gardner DK, Pool TB, Lane M (2000) Embryo nutrition and energy metabolism and its relationship to embryo growth, differentiation, and viability. *Semin Reprod Med* 18: 205–218
- Gu Q, Yang X, Lv J, Zhang J, Xia BO, Kim J-D, Wang R, Xiong F, Meng S, Clements TP et al (2019) AIBP-mediated cholesterol efflux instructs hematopoietic stem and progenitor cell fate. *Science* 363: 1085–1088
- Guibentif C, Rönn RE, Böiers C, Lang S, Saxena S, Soneji S, Enver T, Karlsson G, Woods N-B (2017) Single-cell analysis identifies distinct stages of human endothelial-to-hematopoietic transition. *Cell Rep* 19: 10–19
- Harris JM, Esain V, Frechette GM, Harris LJ, Cox AG, Cortes M, Garnaas MK, Carroll KJ, Cutting CC, Khan T et al (2013) Glucose metabolism impacts the spatiotemporal onset and magnitude of HSC induction *in vivo*. *Blood* 121: 2483–2493
- Imanirad P, Solaimani Kartalaei P, Crisan M, Vink C, Yamada-Inagawa T, de Pater E, Kurek D, Kaimakis P, van der Linden R, Speck N et al (2014) HIF1 α is a regulator of hematopoietic progenitor and stem cell development in hypoxic sites of the mouse embryo. *Stem Cell Res* 12: 24–35
- Isern J, Fraser ST, He Z, Baron MH (2008) The fetal liver is a niche for maturation of primitive erythroid cells. *Proc Natl Acad Sci U S A* 105: 6662–6667
- Ito K, Carracedo A, Weiss D, Arai F, Ala U, Avigan DE, Schafer ZT, Evans RM, Suda T, Lee C-H et al (2012) A PML-PPAR- δ pathway for fatty acid oxidation regulates hematopoietic stem cell maintenance. *Nat Med* 18: 1350–1358
- Ivanovs A, Rybtsov S, Welch L, Anderson RA, Turner ML, Medvinsky A (2011) Highly potent human hematopoietic stem cells first emerge in the intraembryonic aorta-gonad-mesonephros region. *J Exp Med* 208: 2417–2427
- Jing L, Tamplin OJ, Chen MJ, Deng Q, Patterson S, Kim PG, Durand EM, McNeil A, Green JM, Matsuura S et al (2015) Adenosine signaling promotes hematopoietic stem and progenitor cell emergence. *J Exp Med* 212: 649–663
- Kennedy M, Awong G, Sturgeon CM, Ditadi A, LaMotte-Mohs R, Zúñiga-Pflücker JC, Keller G (2012) T lymphocyte potential marks the emergence of definitive hematopoietic progenitors in human pluripotent stem cell differentiation cultures. *Cell Rep* 2: 1722–1735
- Kim PG, Nakano H, Das PP, Chen MJ, Rowe RG, Chou SS, Ross SJ, Sakamoto KM, Zon LI, Schlaeger TM et al (2015) Flow-induced protein kinase A-CREB pathway acts via BMP signaling to promote HSC emergence. *J Exp Med* 212: 633–648
- Kiselev VY, Yiu A, Hemberg M (2018) scmap: projection of single-cell RNA-seq data across data sets. *Nat Methods* 15: 359–362
- Kissa K, Herbomel P (2010) Blood stem cells emerge from aortic endothelium by a novel type of cell transition. *Nature* 464: 112–115
- Lancrin C, Sroczynska P, Stephenson C, Allen T, Kouskoff V, Lacaud G (2009) The haemangioblast generates haematopoietic cells through a haemogenic endothelium stage. *Nature* 457: 892–895
- Medvinsky A, Dzierzak E (1996) Definitive hematopoiesis is autonomously initiated by the AGM region. *Cell* 86: 897–906
- Morgan K, Kharas M, Dzierzak E, Gilliland DG (2008) Isolation of early hematopoietic stem cells from murine yolk sac and AGM. *J Vis Exp* 789
- Moussaieff A, Rouleau M, Kitsberg D, Cohen M, Levy G, Barasch D, Nemirovski A, Shen-Orr S, Laevsky I, Amit M et al (2015) Glycolysis-mediated changes in acetyl-CoA and histone acetylation control the early differentiation of embryonic stem cells. *Cell Metab* 21: 392–402
- Ng ES, Azzola L, Bruveris FF, Calvanese V, Phipson B, Vlahos K, Hirst C, Jokubaitis VJ, Yu QC, Maksimovic J et al (2016) Differentiation of human embryonic stem cells to HOXA+ hemogenic vasculature that resembles the aorta-gonad-mesonephros. *Nat Biotechnol* 34: 1168–1179
- Oatley M, Bölükbası ÖV, Svensson V, Shvartsman M, Ganter K, Zirngibl K, Pavlovich PV, Milchevskaya V, Foteva V, Natarajan KN et al (2020) Single-cell transcriptomics identifies CD44 as a marker and regulator of endothelial to haematopoietic transition. *Nat Commun* 11: 1–18
- Oburoglu L, Mansell E, Woods N-B (2021) Glutamine metabolism regulates endothelial to hematopoietic transition and hematopoietic lineage specification. *Sci Rep* 11: 17589
- Oburoglu L, Tardito S, Fritz V, de Barros SC, Merida P, Craveiro M, Mamede J, Cretenet G, Mongellaz C, An X et al (2014) Glucose and glutamine metabolism regulate human hematopoietic stem cell lineage specification. *Cell Stem Cell* 15: 169–184
- Palis J, Robertson S, Kennedy M, Wall C, Keller G (1999) Development of erythroid and myeloid progenitors in the yolk sac and embryo proper of the mouse. *Development* 126: 5073–5084

- Rahman N, Brauer PM, Ho L, Usenko T, Tewary M, Zúñiga-Pflücker JC, Zandstra PW (2017) Engineering the haemogenic niche mitigates endogenous inhibitory signals and controls pluripotent stem cell-derived blood emergence. *Nat Commun* 8: 1–12
- Renoux VM, Zriwil A, Peitzsch C, Michaëlsson J, Friberg D, Soneji S, Sitnicka E (2015) Identification of a human natural killer cell lineage-restricted progenitor in fetal and adult tissues. *Immunity* 43: 394–407
- Schenk T, Chen WC, Göllner S, Howell L, Jin L, Hebestreit K, Klein H-U, Popescu AC, Burnett A, Mills K *et al* (2012) Inhibition of the LSD1 (KDM1A) demethylase reactivates the all-trans-retinoic acid differentiation pathway in acute myeloid leukemia. *Nat Med* 18: 605–611
- Simsek T, Kocabas F, Zheng J, DeBerardinis RJ, Mahmoud AI, Olson EN, Schneider JW, Zhang CC, Sadek HA (2010) The distinct metabolic profile of hematopoietic stem cells reflects their location in a hypoxic niche. *Cell Stem Cell* 7: 380–390
- Stefanska M, Batta K, Patel R, Florkowska M, Kouskoff V, Lacaud G (2017) Primitive erythrocytes are generated from hemogenic endothelial cells. *Sci Rep* 7: 1–10
- Stein-O'Brien GL, Clark BS, Sherman T, Zibetti C, Hu Q, Sealton R, Liu S, Qian J, Colantuoni C, Blackshaw S *et al* (2019) Decomposing cell identity for transfer learning across cellular measurements, platforms, tissues, and species. *Cell Syst* 8: 395–411.e8
- Street K, Risso D, Fletcher RB, Das D, Ngai J, Yosef N, Purdom E, Dudoit S (2018) Slingshot: cell lineage and pseudotime inference for single-cell transcriptomics. *BMC Genom* 19: 477
- Stuart T, Butler A, Hoffman P, Hafemeister C, Papalexi E, Mauck WM, Hao Y, Stoekius M, Smibert P, Satija R (2019) Comprehensive integration of single-cell data. *Cell* 177: 1888–1902
- Sturgeon CM, Ditadi A, Awong G, Kennedy M, Keller G (2014) Wnt signaling controls the specification of definitive and primitive hematopoiesis from human pluripotent stem cells. *Nat Biotech* 32: 554–561
- Sugimura R, Jha DK, Han A, Soria-Valles C, da Rocha EL, Lu Y-F, Goettel JA, Serrao E, Rowe RG, Malleshaiah M *et al* (2017) Haematopoietic stem and progenitor cells from human pluripotent stem cells. *Nature* 545: 432–438
- Swiers G, Baumann C, O'Rourke J, Giannoulatou E, Taylor S, Joshi A, Moignard V, Pina C, Bee T, Kokkalis KD *et al* (2013) Early dynamic fate changes in haemogenic endothelium characterized at the single-cell level. *Nat Commun* 4: 2924
- Takeuchi M, Fuse Y, Watanabe M, Andrea C-S, Takeuchi M, Nakajima H, Ohashi K, Kaneko H, Kobayashi-Osaki M, Yamamoto M *et al* (2015) LSD1/KDM1A promotes hematopoietic commitment of hemangioblasts through downregulation of Etv2. *Proc Natl Acad Sci U S A* 112: 13922–13927
- Takubo K, Goda N, Yamada W, Iriuchishima H, Ikeda E, Kubota Y, Shima H, Johnson RS, Hirao A, Suematsu M *et al* (2010) Regulation of the HIF-1 α level is essential for hematopoietic stem cells. *Cell Stem Cell* 7: 391–402
- Takubo K, Nagamatsu GO, Kobayashi C, Nakamura-Ishizu A, Kobayashi H, Ikeda E, Goda N, Rahimi Y, Johnson R, Soga T *et al* (2013) Regulation of glycolysis by Pdk functions as a metabolic checkpoint for cell cycle quiescence in hematopoietic stem cells. *Cell Stem Cell* 12: 49–61
- Thambyrajah R, Fadlullah MZH, Proffitt M, Patel R, Cowley SM, Kouskoff V, Lacaud G (2018) HDAC1 and HDAC2 modulate TGF- β signaling during endothelial-to-hematopoietic transition. *Stem Cell Reports* 10: 1369–1383
- Thambyrajah R, Mazan M, Patel R, Moignard V, Stefanska M, Marinopoulou E, Li Y, Lancrin C, Clapes T, Möröy T *et al* (2016) GFI1 proteins orchestrate the emergence of haematopoietic stem cells through recruitment of LSD1. *Nat Cell Biol* 18: 21–32
- Weinreb C, Rodriguez-Fraticelli A, Camargo FD, Klein AM (2020) Lineage tracing on transcriptional landscapes links state to fate during differentiation. *Science* 367: eaaw3381
- Woods N-B, Parker AS, Moraghebi R, Lutz MK, Firth AL, Brennand KJ, Berggren WT, Raya A, Belmonte JCI, Gage FH *et al* (2011) Brief report: efficient generation of hematopoietic precursors and progenitors from human pluripotent stem cell lines. *Stem Cells* 29: 1158–1164
- Yoder MC, Hiatt K, Dutt P, Mukherjee P, Bodine DM, Orlic D (1997) Characterization of definitive lymphohematopoietic stem cells in the day 9 murine yolk sac. *Immunity* 7: 335–344
- Yu WVC, Yusuf RZ, Oki T, Wu J, Saez B, Wang X, Cook C, Baryawno N, Ziller MJ, Lee E *et al* (2016) Epigenetic memory underlies cell-autonomous heterogeneous behavior of hematopoietic stem cells. *Cell* 167: 1310–1322.e17
- Yu W-M, Liu X, Shen J, Jovanovic O, Pohl EE, Gerson SL, Finkel T, Broxmeyer HE, Qu C-K (2013) Metabolic regulation by the mitochondrial phosphatase PTPMT1 is required for hematopoietic stem cell differentiation. *Cell Stem Cell* 12: 62–74
- Yvan-Charvet L, Pagler T, Gautier EL, Avagyan S, Siry RL, Han S, Welch CL, Wang N, Randolph GJ, Snoeck HW *et al* (2010) ATP-binding cassette transporters and HDL suppress hematopoietic stem cell proliferation. *Science* 328: 1689–1693
- Zeng Y, He J, Bai Z, Li Z, Gong Y, Liu C, Ni Y, Du J, Ma C, Bian L *et al* (2019) Tracing the first hematopoietic stem cell generation in human embryo by single-cell RNA sequencing. *Cell Res* 29: 881–894
- Zhou F, Li X, Wang W, Zhu P, Zhou J, He W, Ding M, Xiong F, Zheng X, Li Z *et al* (2016) Tracing haematopoietic stem cell formation at single-cell resolution. *Nature* 533: 487–492



License: This is an open access article under the terms of the Creative Commons Attribution-NonCommercial-NoDeriv License, which permits use and distribution in any medium, provided the original work is properly cited, the use is non-commercial and no modifications or adaptations are made.